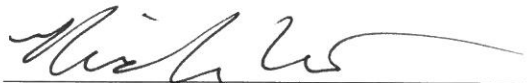
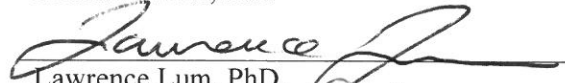


IDENTIFICATION OF ONCOGENIC KRAS-ASSOCIATED VULNERABILITIES  
IN NON-SMALL CELL LUNG CANCER

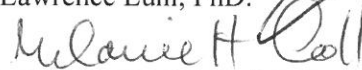
APPROVED BY SUPERVISORY COMMITTEE



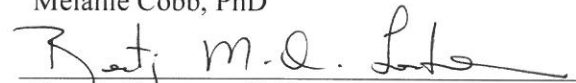
Michael White, PhD



Lawrence Lum, PhD.



Melanie Cobb, PhD



Beatriz Fontoura, PhD

## ACKNOWLEDGEMENTS

I am really grateful that I have had the opportunity to work with so many great people during my PhD, those who have helped me make this achievement. First of all, I would like to thank my mentor, Dr. Michael White, for his insightful guidance and support. I sincerely appreciate the opportunities given to me during my training as a scientist in his lab. I would like to thank my committee members, Drs. Lawrence Lum, Melanie Cobb, Beatriz Fontoura for their expertise, discussions and invaluable feedbacks. I would also like to thank all my collaborators that I mentioned at the end of each chapter. In particular, I am very grateful to Dr. Pier Paolo Scaglioni and Niranjan Venkateswaran for their tremendous support and patience. I would like to thank my bright and compassionate colleagues, current and former members of the White lab, for their help, suggestions, encouragement, and friendship. Particularly, I would like to send my special thanks to Hyunseok Kim, Elizabeth McMillan and Gurbani Makkar for their support and collaboration. I would like to thank my friends for their support and care. It would be a lonely journey without them. In particular, I would like to thank Eunhee Choi, Jiyeon Kim, MiCheong Cheong, HunkarGizem Yesilyurt, and Stacey McCabe.

Finally and most importantly, none of this would have been possible without the love, support and prayers of my family. So I would like to dedicate this work to my loving parents and my husband, Hyun-moo.

IDENTIFICATION OF ONCOGENIC KRAS-ASSOCIATED VULNERABILITIES  
IN NON-SMALL CELL LUNG CANCER

by  
JI MI KIM

DISSERTATION

Presented to the Faculty of the Graduate School of Biomedical Sciences

The University of Texas Southwestern Medical Center at Dallas

In Partial Fulfillment of the Requirements

For the Degree of

DOCTOR OF PHILOSOPHY

The University of Texas Southwestern Medical Center at Dallas

Dallas, Texas

August 2016

Copyright

by

JI MI KIM, 2016

All Rights Reserved

IDENTIFICATION OF ONCOGENIC KRAS-ASSOCIATED VULNERABILITIES  
IN NON-SMALL CELL LUNG CANCER

Publication No. \_\_\_\_\_

Ji Mi Kim, Ph.D.

The University of Texas Southwestern Medical Center at Dallas, 2016

Michael A. White, Ph.D.

Activating mutations in *KRAS* are frequently involved in the pathogenesis of non-small cell lung cancer (NSCLC), the disease responsible for the most cancer-related deaths in the US. Despite intensive efforts to develop drugs that directly interfere with KRAS activity over the past decade, no effective inhibitor has been developed. As an alternative, synthetic-lethal therapeutic opportunities are being pursued using large-scale, RNAi-based, functional genomics platforms. We first addressed two major challenges associated with RNAi-based primary synthetic-lethal screens; a prevalent miRNA-like behavior of siRNA and cell line-dependent phenotypic diversity within intra-lineage *KRAS*-driven cancer. In consideration of these, we performed a whole-genome synthetic-lethal siRNA screen, powered by 106

NSCLC lines and integrated with gene set enrichment analysis. This identified components of nuclear transport machinery as selectively essential for *KRAS* mutant NSCLC lines. We found that pharmacological inhibition of a key nuclear export receptor, XPO1 (a.k.a. CRM1), was sufficient to induce robust and selective apoptosis in *KRAS* mutant NSCLC cells *in vitro* and to cause significant impairment of *KRAS* mutant tumor growth *in vivo*. Mechanistically, XPO1-dependent nuclear export machinery was required to maintain NFκB-mediated survival signaling. We discovered that a subset of *KRAS* mutant NSCLC lines bypassed the addiction to XPO1-dependent nuclear export via YAP1 activation as a consequence of previously unappreciated co-occurring loss-of-function mutations in *FSTL5* and mutations in Hippo pathway. The intrinsic resistance was reversed by coadministration of YAP1/TEAD inhibitor. Thus, our study suggests that XPO1 can be exploited for a promising therapeutic opportunity for *KRAS* mutant lung cancer and provides strategies for genomics-guided application of clinically available XPO1 inhibitors.

## TABLE OF CONTENTS

PRIOR PUBLICATIONS .....	x
LIST OF FIGURES .....	xi
LIST OF DEFINITIONS .....	xiii
 CHAPTER ONE : INTRODUCTION.....	 1
NON-SMALL CELL LUNG CANCER .....	1
REGULATION OF KRAS .....	2
KRAS DOWNSTREAM EFFECTOR SIGNALING.....	4
TARGETING ONCOGENIC KRAS.....	6
ONCOGENIC KRAS AND NF $\kappa$ B SIGNALING .....	8
ONCOGENIC KRAS AND HIPPO SIGNALING EFFECTOR YAP1 .....	10
 CHAPTER TWO: DETECTION OF SEQUENCE-SPECIFIC OFF-TARGET PHENOTYPES FROM WHOLE-GENOME siRNA SCREEN .....	  15
INTRODUCTION.....	15
RESULTS.....	16
DISCUSSION .....	24
MATERIAL AND METHODS .....	25
ACKNOWLEDGEMENTS .....	25

CHAPTER THREE : SELECTIVE ADDICTION TO XPO1-DEPENDENT NUCLEAR  
EXPORT IS A DRUGGABLE VULNERABILITY IN KRAS MUTANT LUNG CANCER.

.....	26
INTRODUCTION.....	26
RESULTS.....	27
DISCUSSION .....	64
MATERIAL AND METHODS .....	67
ACKNOWLEDGEMENTS .....	84

CHAPTER FOUR: CONCLUDING REMARKS.....	86
---------------------------------------	----

BIBLIOGRAPHY .....	87
--------------------	----

## PRIOR PUBLICATIONS

**Kim, J.**, McMillan E., Kim, HS., Venkateswaran, N., Rodriguez-Canales J., Villalobos P., Mendiratta S., Wei S., Landesman Y., Senapedis W., Baloglu E., Chow C.B., Minna JD., Wistuba II., Posner BA., Scaglioni PP., White MA. Selective addiction to XPO1-dependent nuclear export is a druggable vulnerability in *KRAS* mutant lung cancer. *In revision in response to review at Nature*.

Zhong, R. \*, **Kim, J.** \*, Kim, H.S., Kim, M., Lum, L., Levine, B., Xiao, G., White, M.A., and Xie, Y. (2014). Computational detection and suppression of sequence-specific off-target phenotypes from whole genome RNAi screens. *Nucleic acids research*, DOI: 10.1093/nar/gku306 . \*Joint First Authors

Kim H, Mendiratta S, Kim J, Pecot C, Larsen J, Zubovych I, Seo B, **Kim J**, Eskiocak B, Chung H, McMillan E, Wu S, De Brabander J, Komurov K, Toombs J, Wei S, Peyton M, Williams N, Gazdar A, Posner B, Brekken R, Sood A, Deberardinis R, Roth M, Minna M, and White M. A. (2013). Systematic identification of molecular subtype-selective vulnerabilities in non small cell lung cancer. *Cell* 155: 552-66.

Min J., Choi E.S., Hwang K., **Kim J.**, Sampath S., Venkitaraman A.R., Lee H. (2012). The breast cancer susceptibility gene BRCA2 is required for the maintenance of telomere homeostasis. *J Biol Chem* 287(7):5091-101.

Choi E., Choe H., Min J., Choi J.Y., **Kim J.**, Lee H. (2009). BubR1 acetylation at prometaphase is required for modulating APC/C activity and timing of mitosis. *EMBO J*, 28(14), 1991-3.

## LIST OF FIGURES

### CHAPTER 1

Figure 1. 1. KRAS signaling.....	4
Figure 1. 2. NFκB signaling .....	10
Figure 1. 3. Hippo pathway network .....	14

### CHAPTER 2

Figure 2. 1. Detection of 6-mer seed sequences in genome-wide siRNA-based phenotypic screen. ....	19
Figure 2. 2. Viability phenotypes are uncoupled with target gene knock-down. ....	21
Figure 2. 3. miRNA phenocopies siRNA sharing a same seed sequence. ....	23

### CHAPTER 3

Figure 3. 1. Phenotypic diversity among <i>KRAS</i> mutant NSCLC lines .....	39
Figure 3. 2. Synthetic-lethal genetic interactions in <i>KRAS</i> mutant NSCLC cells.....	40
Figure 3. 3. Selective sensitivity of <i>KRAS</i> mutant NSCLC cells to chemical inhibition of the nuclear transport receptor XPO1 .....	42
Figure 3. 4. Ectopic expression of oncogenic KRAS is sufficient to sensitize normal lung epithelia to XPO1 inhibitor. ....	44
Figure 3. 5. Validation of target-specificity of XPO1 inhibitor.....	45
Figure 3. 6. Efficacy and selectivity of KPT-330 <i>in vivo</i> . ....	47
Figure 3. 7. Selective addiction to NFκB activity specifies sensitivity to XPO1 inhibitor. ....	49
Figure 3. 8. IκB depletion is sufficient to confer XPO1 inhibitor resistance to <i>KRAS</i> mutant NSCLC cells.....	51
Figure 3. 9. Selective sensitivity to XPO1 inhibitor is likely due to context-specific consequences of inhibition of NFκB signaling. ....	52

Figure 3. 10. Co-occurring mutations in <i>FSTL5</i> are associated with intrinsic resistance of <i>KRAS</i> mutant lines to XPO1 inhibitor. ....	54
Figure 3. 11. <i>FSTL5</i> mutations detected in cancer cells are loss-of-function mutations and promote resistance to XPO1 inhibitor. ....	55
Figure 3. 12. Association between <i>FSTL5</i> mutation status and YAP1 protein accumulation. ....	57
Figure 3. 13. Intrinsic resistance of <i>KRAS</i> mutant lines to XPO1 inhibitor is associated with YAP1 activation. ....	60
Figure 3. 14. Exceptional responders are accounted for within the mechanistic context of the study as a whole. ....	63

## LIST OF DEFINITIONS

ACC	Acetyl-CoA-Carboxylase
pACC	phospho-Acetyl-CoA-Carboxylase
AICAR	5-Aminoimidazole-4-carboxamide ribonucleotide
AKT	v-Akt murine thymoma viral oncogene homolog
ALK	Anaplastic lymphoma kinase
AMOT	Angiomotin
AMPK	5' AMP-activated protein kinase
AP-1	Activator protein 1
AUC	Area under the curve
Cas9	CRISPR associated protein 9
CCL	Cancer cell line encyclopedia
CK1	Casein kinase 1
CREB	cyclic AMP-responsive element binding protein
CRISPR	Clustered regularly-interspaced short palindromic repeats
ECM	Extracellular matrix
ED50	Median effective dose
EGFR	Epidermal growth factor receptor
ERK	Extracellular regulated kinase
ETS	v-Ets avian erythroblastosis virus E26 oncogene homolog
FSTL5	Follistatin-like 5
GAP	GTPase-activating protein
GDP	Guanosine 5'-diphosphate
GEF	Guanine nucleotide exchange factor
GEM	Genetically engineered model
GFP	Green fluorescent protein
GSEA	Gene set enrichment analysis
GTP	Guanosine 5'-triphosphate
HVR	Hyper-variable region
HBEC	Human bronchial epithelial cell
HCC	Hepatocellular carcinoma
IC50	Half maximal inhibitory concentration
ICMT	Isoprenylcysteine carboxylmethyltransferase

IκB	IkappaB protein
IKK	IκB kinase
IL1b	Interleukin 1, Beta
IQR	Interquartile range
KRAS	Kirsten rat sarcoma viral oncogene homolog
KS-test	Kolmogorov-Smirnov Test
LATS	Large tumor suppressors
LKB1	Liver kinase B1 (STK11)
LPS	Lipopolysaccharide
LUAD	Lung adenocarcinoma
MEK	Mitogen-activated protein kinase kinase
MEKK1	Mitogen-activated protein kinase kinase kinase 1
miRNA	microRNA
MOB1A/B	MOB kinase activator1 A/B
MST1/2	STK4/3, Serine/threonine kinase 4/3
MYC	v-Myc avian myelocytomatosis viral oncogene homolog
NES	Nuclear export signal
NF1	Neurofibromatosis type 1
NF2	Neurofibromatosis type 2, Merlin
NFκB	Nuclear factor kappa-light-chain-enhancer of activated B cells
PAM	Protospacer adjacent motif
PARP	Poly ADP ribose polymerase
PDAC	Pancreatic ductal adenocarcinoma
PDX	Patient-derived xenograft
PI3K	Phosphoinositide-3-kinase
PIK3CA	Phosphatidylinositol-4,5-bisphosphate 3-kinase, Catalytic subunit alpha
PIP2	Phosphatidylinositol-4,5-bisphosphate
PIP3	Phosphatidylinositol-3,4,5-triphosphate
PLCε	Phospholipase C, Epsilon 1
RAF	Raf proto-oncogene, serine/threonine kinase
RALA	v-Ral simian leukemia viral oncogene homolog A
RALB	v-Ral simian leukemia viral oncogene homolog B
RALGDS	Ral guanine nucleotide dissociation stimulator
RASSF	RAS association domain family member 1
RCE1	RAS converting enzyme1
RelA	v-Rel avian reticuloendotheliosis viral oncogene homolog A
RelB	v-Rel avian reticuloendotheliosis viral oncogene homolog B

RGL1	RAL guanine nucleotide dissociation stimulator-like 1
RGL2	RAL guanine nucleotide dissociation stimulator-like 2
RIN1	RAS and RAB interactor 1
RNAi	RNA interference
s.d.	Standard deviation
SAV	Salvador
SCRIB	Scribbled planar cell polarity protein
shRNA	Small hairpin RNA
SOS	Son of sevenless
TAZ	Tafazzin
TCGA	The cancer genome atlas
TEAD	TEA domain family member
TIAM1	T-cell lymphoma invasion and metastasis 1
TNF	Tumor necrosis factor
UTR	Untranslated region
XPO1	Exportin 1
YAP1	Yes-associated protein 1

# **CHAPTER ONE**

## **INTRODUCTION**

### **NON-SMALL CELL LUNG CANCER**

Lung cancer is the leading cause of cancer-related death in the US, responsible for about 1 in 4 cancer deaths with an overall 5-year survival rate of about 20%. It is divided into two main subgroups: small cell lung cancer (SCLC) and non-small cell lung cancer (NSCLC), the latter of which is further subdivided into adenocarcinoma, squamous cell carcinoma, and large cell carcinoma, based on histological appearance. NSCLC accounts for most of lung cancer (85%). Early-stage NSCLC usually undergoes surgical resection, sometimes coupled with chemotherapy and radiation therapy. For advanced-stage cancer, treatment involves chemotherapy, targeted therapy, and/or immunotherapy (American Cancer Society, 2016).

Traditionally, treatment decision for lung cancer patients has been made simply based on histology. However, the recent advances in genomics have allowed us to identify somatic alterations that frequently occur in NSCLC (Cancer Genome Atlas Research, 2012, 2014). This has spurred the efforts to develop treatments that incorporate molecular subtypes involving the somatic alterations (Pao and Hutchinson, 2012; Roberts and Stinchcombe, 2013). For example, the identification of activating *EGFR* mutations in NSCLC and the subsequent development of EGFR tyrosine kinase inhibitors, erlotinib and gefitinib, led to significant survival benefits, emphasizing the importance of tailored therapies targeting

particular molecular subtypes defined by genetic mutations (Roberts and Stinchcombe, 2013).

Comprehensive molecular profiling has identified major somatic alterations in NSCLC including mutations in *KRAS*, *EGFR*, *ALK*, *BRAF*, *PIK3CA*, and *AKT1*. Among them, activating mutations in *KRAS* is the most frequent, which have been detected in ~30% of NSCLC (Cancer Genome Atlas Research, 2014).

## **REGULATION OF KRAS**

KRAS is 21kDa small GTPase that cycles between GDP-bound inactive state and GTP-bound active state and regulates cell proliferation, differentiation and survival by interacting with multiple downstream effectors (Jancik et al., 2010). *KRAS* encodes highly related two variants, KRAS 4A and 4B, resulting from alternative splicing of exon 4. They share identical sequences in the first 168-169 amino acids, which are known as G-domain, and diverge in their C-terminal 20 amino acids, which are named hyper-variable region (HVR). G-domain is responsible for binding GDP/GTP and interacting with downstream effectors, guanine exchange factors (GEFs) and GTPase-activating proteins (GAPs). HVR is required for membrane localization of KRAS protein (Ahearn et al., 2012; Jancík et al., 2010; Tsai et al., 2015). KRAS 4B is a dominant isoform that expresses ubiquitously.

Once KRAS is translated in the cytoplasm, HVR of KRAS protein undergoes a series of post-translational modifications. HVR harbors CAAX motif, which is modified by several enzymes. Firstly, farnesyltransferase adds farnesyl lipid to cysteine residue on CAAX motif.

This results in KRAS accumulation on the cytoplasmic face of the endoplasmic reticulum, where KRAS sequentially associates with RAS-converting enzyme 1 (RCE1) and isoprenylcysteine carboxylmethyltransferase (ICMT). RCE1, an endoprotease, removes the AAX amino acids of the CAAX motif and then ICMT methylesterifies the carboxyl group of the farnesylcysteine. Then, KRAS 4B directly processes to the plasma membrane via electrostatic interaction between its polylysine region and negatively charged region of the plasma membrane while KRAS 4A undergoes another modification, palmitoylation at Cys180 via palmitoyltransferase and then reaches to the membrane via the conventional Golgi secretory pathway(Ahearn et al., 2012).

At the plasma membrane, KRAS is activated by guanine exchange factors (GEFs), which catalyze exchange of GDP to GTP. Activated KRAS promotes cell proliferation, differentiation and survival by engaging various downstream effectors. KRAS inactivation is induced by hydrolysis of GTP to GDP. The intrinsic GTPase activity of KRAS is very weak and this step is facilitated by GTPase-activating proteins (GAPs). In mammals, 8 RAS-GEFs including 2 isoforms of SOS, and 7 RAS-GAPs including P120RASGAP and NF1 have been identified (Figure 1.1) (Ahearn et al., 2012; Karnoub and Weinberg, 2008). The oncogenic mutations in *KRAS* primarily occur at residues G12, G13 and Q 61. They impair intrinsic and GAP-mediated GTP hydrolysis and render KRAS persistently active, thereby activating downstream effector pathways and mediating malignant cellular transformation(Gysin et al., 2011).

## KRAS DOWNSTREAM EFFECTOR SIGNALING

At least 7 effector proteins have been identified: RAF, PI3K, RALGEF, PLC $\epsilon$ , TIAM1, RASSF, and RIN1. They interact with KRAS in a GTP-dependent manner, activating downstream signaling cascades and affecting several important cellular processes (Figure 1.1). Among them, the first three have been the most extensively studied.

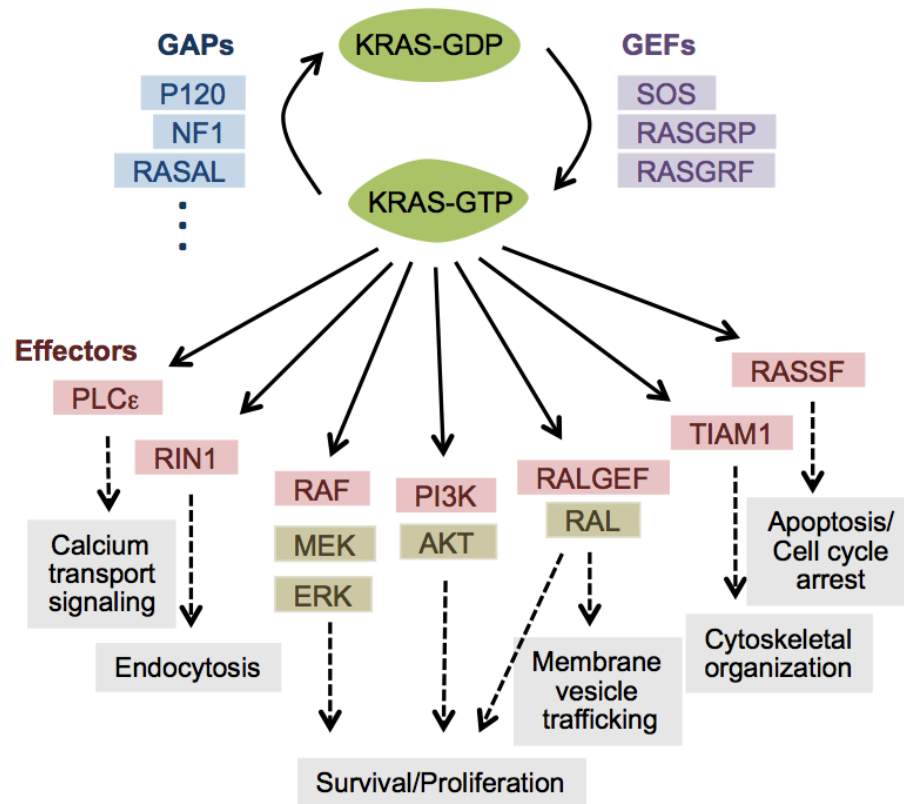


Figure 1. 1. KRAS signaling

### RAF/MEK/ERK signaling

RAF serine/threonine kinase is the first identified effector. In mammalian cells, RAF family consists of RAF1, A-RAF and B-RAF. They share three domains: CR1 (the RAS binding domain), CR2 (the regulatory domain), and C3 (the kinase domain). All of them can activate downstream targets by phosphorylation, but they have different biochemical potencies (B-RAF>RAF1>>A-RAF) (Chang et al., 2003). RAF is activated by recruitment to the plasma membrane through binding to oncogenic KRAS and by subsequent phosphorylation on different domains via different kinases. Activated RAF phosphorylates and activates MEK1/2, which results in phosphorylation and activation of ERK1/2. This cascade is relayed to a set of transcription factors including CREB, ETS, AP-1 and MYC and regulates cell proliferation and survival (Chang et al., 2003).

### PI3K/AKT signaling

PI3K is a heterodimeric lipid kinase that consists of catalytic subunit and regulatory subunit. In mammalian cells, there are 3 main classes in the PI3K family (class I, II and III). Class I PI3K is the best characterized and the most implicated in human cancer (refer to PI3K in subsequent text). The catalytic subunits of PI3Ks are composed of class 1A group (p110 $\alpha$ , p110 $\beta$ , and p110 $\delta$ ) which interact with p85 regulatory subunit, and class 1B group (p110 $\gamma$ ) which binds to either p101 or p87 regulatory subunit. Oncogenic KRAS activates p110 subunit, resulting in generation of the signaling molecule PIP3 from PIP2. PIP3 directly binds to AKT, which leads to AKT phosphorylation on Thr308 and Ser473 by upstream kinases. Activated AKT propagates cell survival and proliferation signaling through

phosphorylation of numerous downstream targets(Castellano and Downward, 2011; Vanhaesebroeck et al., 2012).

#### RALGEF-RAL effector signaling

RALGEF is a guanine nucleotide exchange factor that has selectivity for RALA and RALB. KRAS can bind to and activate 4 members of RALGEF family: RALGDS, RGL1, RGL2 and RGL3. Activated RALGEF regulates RAL effector activity via facilitating the transition of RAL-GDP to RAL-GTP. RALA and RALB are small GTPase that are originally identified based on their sequence homology to RAS family and are found to express ubiquitously in human. Even though RALA and RALB share about 80% of sequence identity, they play distinct functional roles in cancer. It was shown that RALA is required for anchorage-independent proliferation while RALB is essential for survival of tumor cells but not normal cells(Chien and White, 2003). GTP-bound RALs interact with multiple downstream effectors and regulate different biological processes including vesicle trafficking (Bodemmann and White, 2008).

### **TARGETING ONCOGENIC KRAS**

Based on the comprehensive understanding of molecular requirement for KRAS activity, attempts to intercept oncogenic KRAS activity have been made in the past decades.

However, direct inhibition of KRAS has proven to be unsuccessful because of picomolar affinity of KRAS protein for guanine nucleotide, the abundance of GTP in a micromolar range, and lack of an accessible drug binding site(Gysin et al., 2011). Recent studies have

shown that at least one subtype of mutant KRAS can be chemically targeted. Kevan Shokat group identified compounds that specifically react with cysteine residue at codon 12 of GDP-bound KRAS<sup>G12C</sup>, resulting in GDP-bound, inactive mutant KRAS accumulation (Ostrem et al., 2013). Nathanael Gray group developed a GDP analogue that selectively binds to KRAS<sup>G12C</sup> via a covalent interaction and competes for the GTP binding pocket (Lim et al., 2014). Given that intrinsic KRAS GTPase activity can exert GTP-GDP cycling even though G12 mutation impairs GAP-mediate hydrolysis, allele-specific inhibitors suggest potential therapeutic opportunities but further studies are likely necessary to overcome bioavailability issues of the inhibitors.

Abrogation of post-translational modification of KRAS and its localization to the plasma membrane has been considered as a therapeutic strategy for *KRAS* mutant cancer. Farnesylation is the first and irreversible step of post-translational modifications that KRAS undergoes for its membrane localization and was exploited for inhibition of KRAS activity. However, farnesyltransferase inhibitor failed to show efficacy in clinical trials because of alternative modification that compensates farnesylation inhibition (Rowell et al., 1997). Nevertheless, recent studies have suggested the possibility of targeting other steps of post-translational modifications and targeting proper membrane trafficking of farnesylated KRAS (Stephen et al., 2014). For example, Herbert Waldmann group showed that small molecule-mediated inhibition of PDE $\delta$ , a prenyl-binding protein that facilitates release of KRAS4B from the Golgi and its localization to the plasma membrane, suppresses

proliferation of oncogenic *KRAS*-driven PDAC cells and impairs ERK signaling (Zimmermann et al., 2013).

As an alternative of direct interference of *KRAS* activity, a great deal of efforts has been directed to develop therapies by inhibiting downstream effector pathways. Several inhibitors of major components of *KRAS* downstream signaling cascades have been developed and evaluated in clinical trials. Recently, dual-inhibition targeting two major downstream signaling pathways, RAF/MEK/ERK and PI3K/AKT, has been extensively under investigation (Singh et al., 2015). In addition, several groups have sought therapeutic opportunities by investigating synthetic-lethal vulnerabilities in *KRAS* mutant cancer. Synthetic lethality can occur when somatic alterations in cancer create collateral vulnerability to second perturbations. Large-scale RNAi screens have been employed to identify genes whose depletion results in a lethal effect on *KRAS* mutant cells but not wild-type cells (Barbie et al., 2009; Corcoran et al., 2013; Luo et al., 2009; Scholl et al., 2009).

## **ONCOGENIC KRAS AND NFκB SIGNALING**

NFκB transcription factor serves as an important regulator for expression of a variety of genes essential for cell immunity, survival and differentiation. Five proteins have been identified as members of the NFκB family: RELA(p65), RELB, c-REL, p50/p105, p52/p100. These proteins bind to specific DNA sequences as a homodimer or a heterodimer and regulate target gene transcription both positively and negatively (Gerondakis et al., 1999; May and Ghosh, 1998). Genetic approaches in mice have shown that mice deficient in

multiple NF $\kappa$ B proteins displayed novel phenotypes or more severe phenotypes than those observed in single mutants, suggesting that these proteins are functionally redundant (Gerondakis et al., 1999).

In most quiescent cells, the dimers are sequestered in the cytoplasm through association with inhibitory proteins called I $\kappa$ Bs. Among 7 I $\kappa$ B proteins identified, I $\kappa$ B $\alpha$  has been the most extensively studied. In the classical pathway, NF $\kappa$ B activation is achieved by rapid degradation of I $\kappa$ B $\alpha$  proteins followed by I $\kappa$ B $\alpha$  phosphorylation via I $\kappa$ B Kinases and ubiquitination. Released NF $\kappa$ B translocates to the nucleus and activates target gene expression (Figure 1.1)(Hayden and Ghosh, 2012; Oeckinghaus et al., 2011). The NF $\kappa$ B activation is transient in most cases and tightly regulated by negative feedback mechanisms. I $\kappa$ B $\alpha$  is resynthesized by NF $\kappa$ B transcriptional activation. The newly synthesized I $\kappa$ B $\alpha$  inhibits further nuclear translocation of NF $\kappa$ B in the cytoplasm and also enters the nucleus and displaces NF $\kappa$ B dimers from DNA (Beg and Baldwin, 1993).

I $\kappa$ B Kinase complex is responsible for I $\kappa$ B phosphorylation and is activated by a variety of physiologic stimuli including TNF $\alpha$ , LPS and IL1 $\beta$  (Hoesel and Schmid, 2013) and oncogenic signals (Staudt, 2010) .

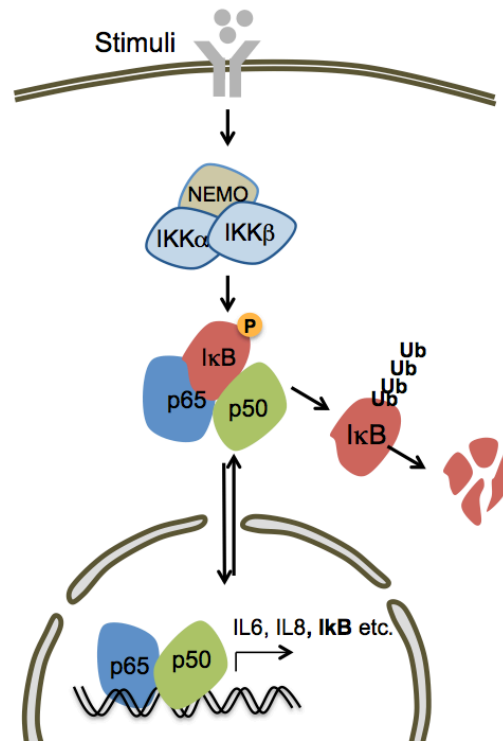


**Figure 1. 2. NFκB signaling pathway**

It has been shown that NFκB signaling pathway can be activated by oncogenic KRAS and is essential for oncogenic *KRAS*-driven tumor initiation and maintenance. Several groups showed that *Kras* mutant mouse cells induced cell death in response to NFκB inhibition by shRNA or expression of degradation-resistant form of IκBα (Mayo et al., 1997; Meylan et al., 2009). Similarly, using *Kras*<sup>G12D</sup>/*p53*<sup>-/-</sup> mouse model, it was demonstrated that *RelA*(p65) null mice and mice engineered to express degradation-resistant IκBα displayed significantly lower lung tumor burden in response to oncogenic *Kras* induction as compared to counterpart control mice (Basseres et al., 2010; Meylan et al., 2009). Previously, mechanistic links between RAS signaling pathway and NFκB were identified. It was found that RAS

downstream effector, RAF promotes NF $\kappa$ B activity in cooperation with MEKK1 through phosphorylating IKK (Baumann et al., 2000) and AKT directly phosphorylates IKK $\alpha$  to induce NF $\kappa$ B activation (Bai et al., 2009). Recently, William Hahn's group showed that oncogenic KRAS activates NF $\kappa$ B signaling through TBK1, a non-canonical I $\kappa$ B Kinase (Barbie et al., 2009). Paul Chiao group reported that oncogenic KRAS induces AP-1-mediated IL1 $\alpha$  overexpression and in turn activates NF $\kappa$ B (Ling et al., 2012).

### **ONCOGENIC KRAS AND HIPPO SIGNALING EFFECTOR YAP1**

Recently YAP1 has been recognized as an important factor in KRAS dependent cancers for their survival upon oncogenic *KRAS* inactivation. Recent studies revealed that 1) gain of Yap1 function was responsible for tumor recurrence after loss of oncogenic Kras in mice model of pancreatic and lung cancers (Kapoor et al., 2014; Shao et al., 2014a) and that 2) increased YAP1 level is associated with worse response to RAS signaling targeted therapies including RAF/MEK inhibitors in NSCLC and melanoma (Lin et al., 2015a).

#### Hippo signaling effector YAP1

YAP1 is a major downstream effector of Hippo tumor suppressor pathway, which regulates cell growth, organ size, and tissue homeostasis. In mammals, TAZ, a paralog of YAP1, also serves as a downstream effector of Hippo signaling and shares many aspects of function and regulatory mechanism with YAP1 (Varelas, 2014). The upstream core components of Hippo pathway consist of serine-threonine kinases, MST1/2 and LATS1/2. When Hippo signaling is

on, MST1/2, in complex with scaffolding protein SAV1, phosphorylate and activate LATS1/2 and their cofactors, MOB1A/B. Activated LATS in turn phosphorylate YAP1/TAZ and regulate their subcellular localization and stability. When Hippo signaling is off, YAP1/TAZ accumulate in the nucleus and form complexes with transcription factors to regulate target gene expression (Johnson and Halder, 2014).

#### Post-translational regulation of YAP1

YAP1 has five LATS target consensus motifs (HxRxxS). Phosphorylation of YAP1 on serine 127 allows 14-3-3 protein to bind to YAP1, resulting in cytoplasmic retention of YAP1. Phosphorylation of YAP1 on serine 381 primes YAP1 for subsequent phosphorylations on serine residues 400 and 403 by CK1 $\delta/\epsilon$ , resulting in recruitment of SCF E3 ubiquitin ligase, which induces YAP1 ubiquitination and proteasome-mediated degradation (Zhao et al., 2010b). The physiological function of phosphorylations on the remaining sites (serine 61, serine 109, and serine 164) still remains to be elucidated. Kun-Liang Guan group showed that the oncogenic potential of phosphorylation-defective YAP15SA mutant (S61A, S109A, S127A, S164A, S381A) is abolished by restoring either one of serine residues 127 or 381 (Zhao et al., 2009).

In addition to LATS, other kinases can phosphorylate and regulate YAP1. It was shown that AKT phosphorylates YAP1 at serine 127 and promotes its cytoplasmic localization (Basu et al., 2003); c-ABL kinase and SRC family kinases (SRC and YES) trigger YAP1 phosphorylation at tyrosine 357 in response to different stimuli and stabilize YAP1 (Levy et

al., 2008; Taniguchi et al., 2015); AMPK phosphorylates YAP1 at serine 94, resulting in disruption of the YAP1-TEAD complex (Mo et al., 2015).

#### Nuclear function of YAP1

As a transcription co-activator, YAP1 mediates the biological functions of Hippo pathway by interacting with transcription factors and regulating gene expression. TEAD family transcription factors (TEAD1-4) were identified as the most potent transcription factors mediating YAP1 function from a luciferase-based YAP1 transcription activity screen (Zhao et al., 2008). In addition, chromatin immunoprecipitation with a YAP1 antibody followed by sequencing revealed that the known TEAD consensus motif (CATTCC) was enriched in YAP1 binding sites (Stein et al., 2015). Besides TEADs, YAP1 has been shown to bind to other transcription factors including  $\beta$ -catenin, SMAD, p73, and TBX5 (Varelas, 2014). Several independent studies have conducted whole-genome transcript profiling to define YAP1 target genes (Lin et al., 2015a; Lin et al., 2015b; Shao et al., 2014b). However, the overlap between the gene expression signatures from the studies is not high, suggesting that regulation of target gene expression by YAP1 is context-dependent and different sets of genes work together to exert biological functions of YAP1 in a context-specific manner (Yu et al., 2015a).

#### Hippo pathway regulation by multiple inputs

Hippo signaling - ultimately YAP1/TAZ - is interconnected with and regulated by several regulators (Figure 1.2)(Yu et al., 2015b): 1) molecules at cell to cell junction including Merlin, SCRIB (which directly interact with LATS and promote their activity), AMOT, and

$\alpha$ -catenin (which inhibit YAP1/TAZ function by sequestering them to cell junctions) (Yu et al., 2015b); 2) mechanical cues such as ECM stiffness and cell-cell contact (which engage Rho GTPase activity and increase tension of actin cytoskeleton, resulting in YAP1/TAZ activation)(Dupont et al., 2011; Yu et al., 2012); 3) ligand-mediated signals through G-protein coupled receptors(GPCRs) (which regulate YAP1/TAZ via possibly Rho GTPase/actin cytoskeleton organization)(Yu et al., 2012); 4) metabolic stress(which inhibits YAP1/TEAD interaction by inducing AMPK-mediated phosphorylation on YAP1 and increases LATS activity)(Mo et al., 2015).

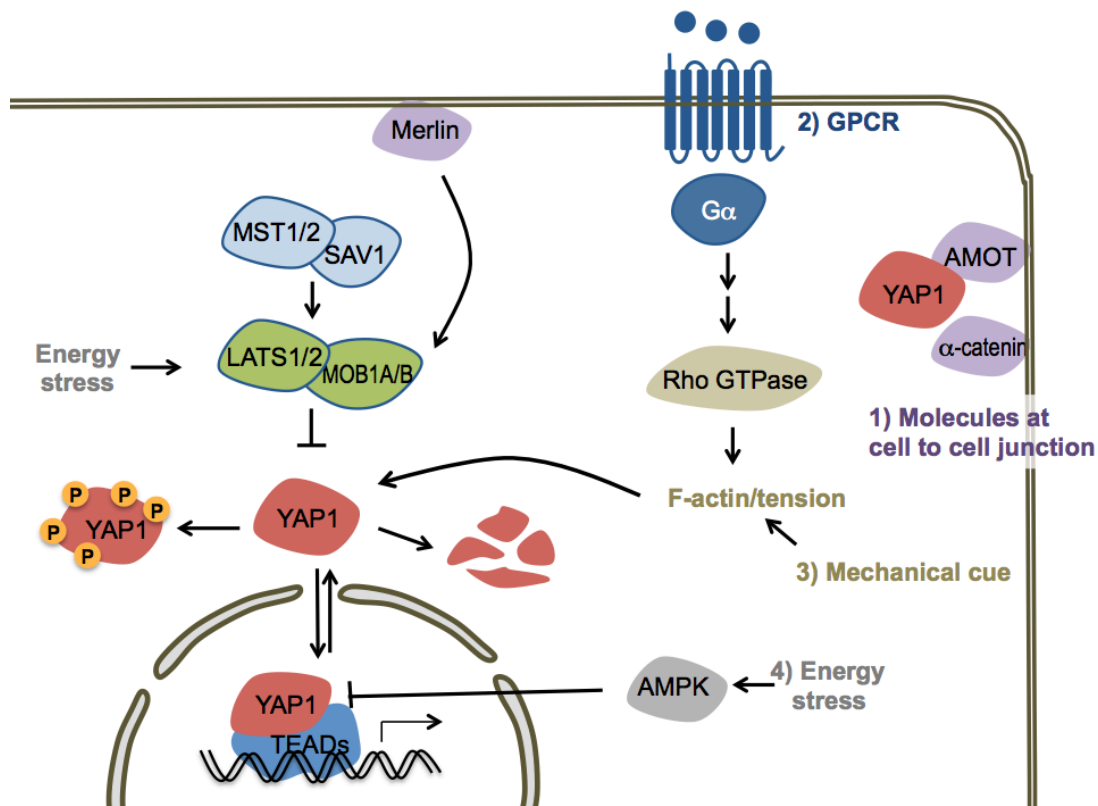


**Figure 1. 3. Hippo pathway network**

## CHAPTER TWO

### DETECTION OF SEQUENCE-SPECIFIC OFF-TARGET PHENOTYPES FROM WHOLE-GENOME siRNA SCREEN

#### INTRODUCTION

Short interference RNA (siRNA) is a 19-22nt RNA fragment that induces post-transcriptional gene silencing(Elbashir et al., 2001) and has become a powerful method of studying loss-of-function phenotypes. Large-scale silencing studies using this tool have been widely performed to identify drug targets in disease contexts. Examples are synthetic-lethal screening efforts to identify molecular vulnerabilities selectively created in *KRAS* mutant cancer cells (Kumar et al., 2012; Sarthy et al., 2007). It has been believed that siRNA can silence genes only when the sequences are perfectly complemented. However, recent studies have shown that siRNA often interferes with the expression of hundreds of unintended transcripts through partial sequence complementarity via miRNA-like mode of action (Doench et al., 2003; Jackson et al., 2006; Lin et al., 2005; Marine et al., 2012; Zhong et al., 2014).

MicroRNA (miRNA) is a small non-coding RNA that shares structural similarity with siRNA. It is endogenously transcribed as a long RNA which undergoes a series of cleavage events by RNaseIII processing enzymes to form ~22nt mature miRNA. In most cases, miRNA binds to the 3' UTR of multiple target mRNAs through “seed sequence”-mediated

partial complementarity (He and Hannon, 2004). Seed sequence is a 6-nucleotide sequence located at positions 2-7 from the 5' end of miRNA (Bartel, 2009).

Due to the miRNA characteristic of having multiple targets, the miRNA-like mode of action of siRNA can cause high-false positive rate, confounding the gene-level interpretation of large-scale siRNA screens. Therefore, deconvolution of off-target phenomena is important to maximize the return of gene level information. Using a KS-test as a scoring metric, we addressed this issue in our whole-genome siRNA primary screen. We systematically identified 6-nucleotide seed sequences in siRNA oligonucleotides associated with a significant Z score distribution bias and we empirically validated miRNA-like behavior of siRNAs.

## RESULTS

We employed our genome-wide siRNA-based phenotypic screen to examine an unintentional effect of siRNAs. The siRNA screen was performed using a high-throughput one-gene/one-well screening platform with pooled siRNA libraries from Ambion and Dharmacon (Figure 2.1A). The cell viability for each siRNA pool was converted to a Z score from a triplicate analysis and was subjected to a two-sample KS-test to detect sequence-specific effects based on the coherent behavior of groups of siRNA pools with oligos sharing a common seed sequence. The KS test determines the maximum distance between the cumulative distribution of the Z scores of siRNA pools containing same 6-mer at their seed region (seed family,

afterwards) and the cumulative distribution of the *Z* scores of the remaining siRNA pools (background, afterwards). If the two distributions are significantly different (KS *P* value<0.05), the 6-mer was considered as an off-target seed sequence (Figure 2.1B). Seed families were separately defined for each of the 6-mer windows present within each 19-mer and examined for their seed sequence/phenotype associations. Off-target seed sequences were detected only in seed families defined by nucleotide positions 1-6, 2-7, and 3-8. Of note, they were highly enriched in seed families defined by nucleotide positions 2-7, which correspond to the canonical miRNA seed region (Figure 2.1C).

By examining our whole-genome siRNA screen performed with siRNA pools in HCC4017, we identified 33 off-target seed sequences that caused collectively significant cell viability phenotypes as compared to background and resulted in a *Z* score distribution bias. For empirical validation of the off-target seed effect of siRNAs, individual oligos targeting 62 genes were further examined for their effect on cell viability in HCC4017. The result showed that siRNA oligos containing the off-target seed sequences exhibited stronger cell viability phenotypes than siRNAs targeting the same sequences (Figure 2.2A, B). To test if the seed sequence/phenotype association is driven by the off-target seed sequence or caused by different knock-down efficiency of the individual oligos, 4 genes were chosen and their transcript expressions were measured after transfection of the individual siRNA oligos. All the individual oligos efficiently silenced the corresponding target gene mRNA (Figure 2.2C),

suggesting that the observed toxic phenotype is oligo sequence-specific, but not target gene-dependent.

Among the off-target seed sequences I tested, UCUGAC was found at the seed region of the previously annotated miRNA, has-miR-4256 (Figure 2.3A). To confirm the miRNA-like mode of action of siRNA, I transfected miR-4256 and siRNA sharing the same seed sequence to HCC4017 in parallel and examined consequence on cell viability. As expected, they displayed similar viability phenotypes. I further tested the seed sequence-driven phenotype by generating the synthetic miRNA that harbors non-toxic negative control oligonucleotide sequences with off-target seed ACAUGU at its seed region (Figure 2.3A). Remarkably, the replacement of 6-mer at the seed region with off-target seed sequence was sufficient to make the non-toxic oligo into a toxic reagent (Figure 2. B,C).

**Figure 2. 1**

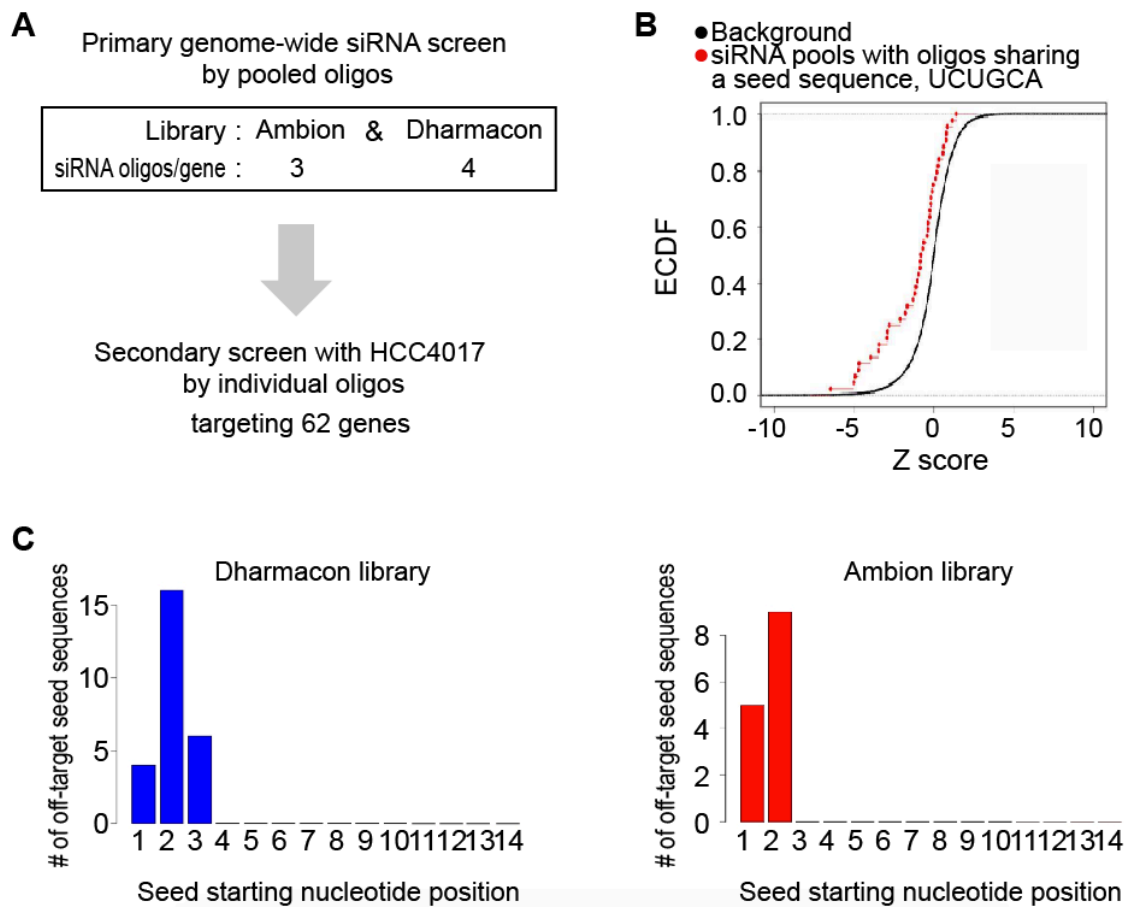


**Figure 2.1. Detection of 6-mer seed sequences in genome-wide siRNA-based phenotypic screen.** (A) Schematic of siRNA screen (B) Illustration of statistical detection of off-target seed sequences in the screen using a KS-test as a scoring metric. If the Z score distribution of siRNA pools with oligos sharing a common 6-mer seed sequence (Red) is statistically different (KS  $P$  value  $<0.05$ ) from the Z score distribution of the remaining siRNA pools (Black), the 6-mer sequence is considered as an off-target seed sequence. (C) Off-target seed sequences were enriched in seed families defined by nucleotide positions 2-7 that correspond to the miRNA seed region.

Figure 2. 2

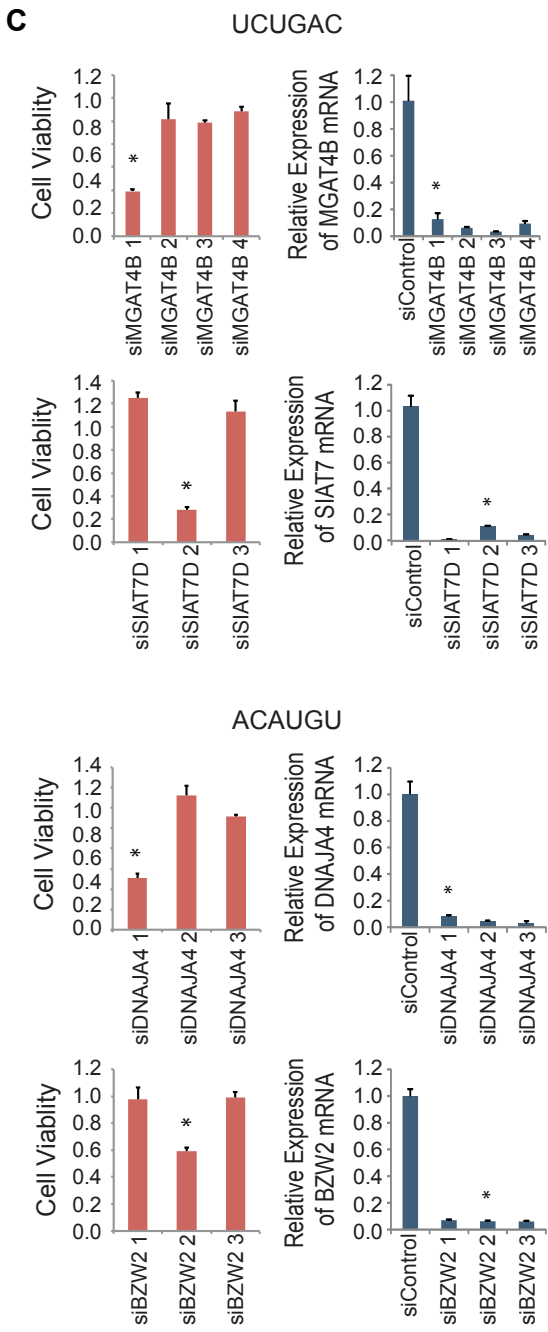
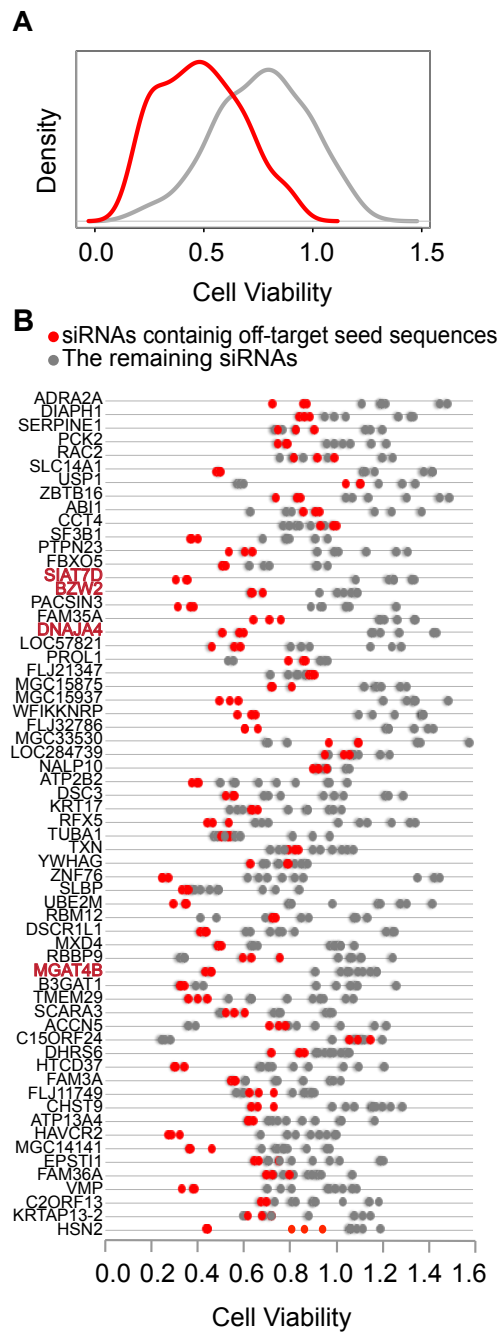


**Figure 2.2. Viability phenotypes are uncoupled with target gene knock-down.**

(A) Density distribution of cell viability in response to individual siRNAs targeting 62 genes. Red: siRNAs harboring off-target seed sequences, Grey: the rest of the siRNAs. (B) Cell viability triplicate values for the individual siRNAs. The siRNAs harboring off-target seed sequences (Red dots) are more toxic than the siRNAs targeting the same gene but without seed sequences (grey dots). The genes chosen for further analysis are indicated in red. (C) Cell viability and target gene expression in response to individual oligos. Cell viability plots (left panels) were generated from (B). The siRNAs containing off-target seed sequences are indicated with asterisk. Bars indicate mean of triplicates + s.d.

**Figure 2. 3**

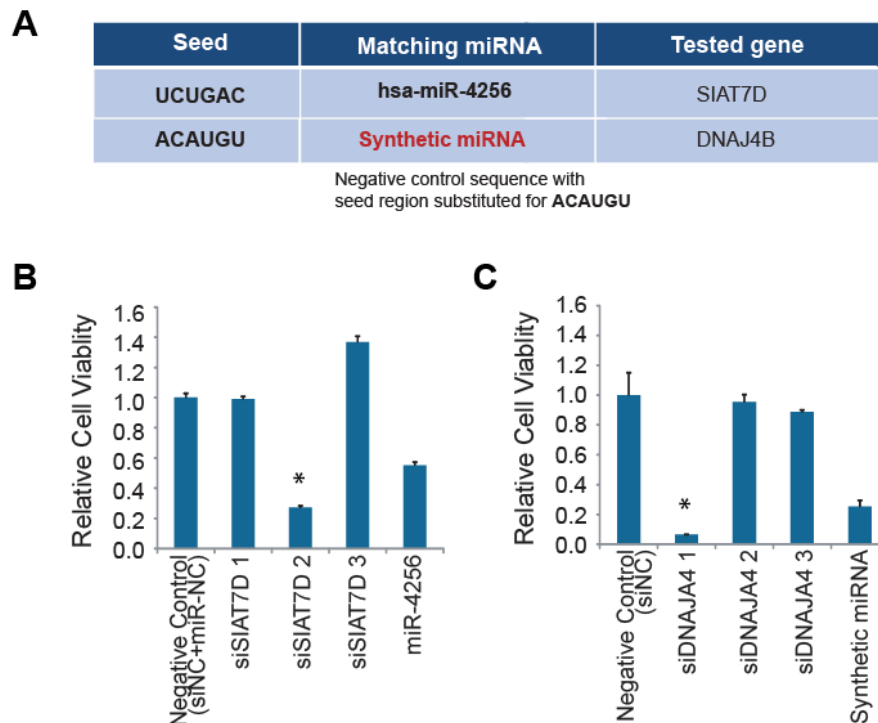


**Figure 2.3. miRNA phenocopies siRNA sharing a same seed sequence.**

(A) Two off-target seed sequences identified in our analysis and two miRNAs harboring the off-target seed sequences at the seed region. The synthetic miRNA was designed to harbor non-toxic negative control oligonucleotide sequences with off-target seed ACAUGU at its seed region. (B) The oligonucleotide mimic of has-miR-4256 containing off-target seed sequence UCUGAC significantly reduced cell viability. The siRNA oligo with the off-target seed is indicated with asterisk. Bars indicate mean of triplicates + s.d. (C) The synthetic miRNA designed to harbor off-target seed sequence in negative control backbone significantly reduced cell viability. The siRNA oligo with the off-target seed is indicated with asterisk. Bars indicate mean of triplicates + s.d.

## DISCUSSION

Using a non-parametric two sample KS-test as a scoring metric, we systematically identified off-target seed sequences in our whole-genome siRNA screening data. We experimentally validated that the siRNA oligonucleotides containing the seed sequences resulted in sequence specific, but not target gene knock-down dependent, toxic phenotypes via miRNA-mimic mode of action. Previously it was found that siRNAs targeting the same transcript but harboring different sequences caused different consequence on cell viability and distinct expression profiles (Jackson et al., 2003; Lin et al., 2005). We provided evidence that siRNA can behave as miRNA by demonstrating that miRNA and siRNA sharing the same sequence at the seed region resulted in the same cellular phenotypic consequence. Most strikingly, we showed that replacement of 6-mer at the seed region with an off-target seed sequence was sufficient to make non-toxic negative control oligos into toxic reagents, suggesting that the observed viability phenotype in our analysis was indeed caused by off-target seed sequences. The seed sequence-mediated siRNA off-target effect can confound efforts to annotate functions of protein-coding genes and to discover drug targets in siRNA screens. To address seed sequence-driven false positives and enrich biologically relevant information in large-scale siRNA screens, our group and collaborators developed a computational tool called DecoRNAi (Deconvolution Analysis of RNAi screening data). It can simultaneously estimate on-target effects and off-target effects based on deconvolution of phenotypic measurements from whole-genome siRNA screening data (Zhong et al., 2014).

Furthermore, our results suggest that the miRNA-like behavior of siRNA can be utilized to identify novel miRNAs that have anti-proliferative activity in large-scale siRNA screens. The off-target seed sequences across 12 NSCLC cell lines are available from our whole-genome siRNA screen. This offers an opportunity to detect molecular subtype-specific off-target seed sequences and corresponding miRNAs that function as tumor suppressors in NSCLC.

## **MATERIAL AND METHODS**

Comprehensive information for tissue culture, oligo transfection, cell viability assay and targeted gene expression analysis is provided in MATERIAL AND METHODS of CHAPTER 3. The miR-4253 and the synthetic miRNA were purchased from Ambion. Non-targeting miRNA control (IN-001005-01-05) was from Dharmacon.

## **ACKNOWLEDGEMENTS**

I wish to thank Hyunseok Kim, Saurabh Mendiratta, Shuguang Wei and HTS core for primary whole-genome siRNA screening and secondary individual siRNA screening efforts; Hyunseok Kim and Rui Zhong for computational analysis of off-target seed sequences for Figure 2.1, 2.2.

## CHAPTER THREE

### SELECTIVE ADDICTION TO XPO1-DEPENDENT NUCLEAR EXPORT IS A DRUGGABLE VULNERABILITY IN KRAS MUTANT LUNG CANCER

#### INTRODUCTION

The common participation of oncogenic KRAS proteins in many of the most lethal of human cancers, together with the ease of detecting somatic *KRAS* alleles in patient samples, has spurred persistent and intensive efforts to develop drugs that intercept KRAS activity. However, the clinical impact of such efforts has been hindered by pervasive inter- and intra-lineage diversity of the targetable mechanistic etiology underpinning KRAS-driven cancers; limited pharmacological accessibility of many candidate synthetic-lethal interactions; and ready emergence of unanticipated resistance mechanisms to otherwise effective targeted therapies. Here we demonstrate specific cell-autonomous addiction of *KRAS* mutant non-small cell lung cancer to receptor-dependent nuclear export. A multi-genomic data-driven approach, powered by 106 NSCLC lines, was used to interrogate 4725 biological processes with 39,760 siRNA pools for those selectively required for survival of KRAS mutant NSCLC lines additionally harboring a broad spectrum of collateral phenotypic variation. Multiple components of the nuclear transport machinery were the sole process-level discriminators reaching statistical significance. XPO1 is a key nuclear export receptor, which mediates

export of nuclear exporting signal (NES)-containing nuclear proteins to the cytoplasm. Chemical perturbation of XPO1, with a clinically available drug, revealed a robust synthetic-lethal interaction with native or engineered oncogenic KRAS expression *in vitro* and *in vivo*. The primary mechanism underpinning XPO1 inhibitor sensitivity was determined to be intolerance of accumulation of nuclear I $\kappa$ B with consequent inhibition of NF $\kappa$ B transcription factor activity.

Of note, we identified a subset of *KRAS* mutant NSCLC lines that bypassed the addiction to XPO1-dependent nuclear export. From the cohort, we discovered previously unappreciated co-occurring loss-of-function mutations in *FSTL5* that specify resistance to XPO1 inhibitors in *KRAS* mutant NSCLC cells. Loss of *FSTL5* resulted in YAP1 induction, and YAP1 activation was sufficient to confer resistance to XPO1 inhibitor in otherwise sensitive *KRAS* mutant lines. This resistance mechanism is predicted to occur in approximately 17% of *KRAS* mutant lung cancers, and can be defeated by coadministration of the YAP1/TEAD inhibitor. Thus, clinically available XPO1 inhibitors present as a promising therapeutic strategy for a significant cohort of lung cancer patients when coupled to genomics-guided patient selection and monitoring.

## RESULTS

In response to the acute therapeutic need, extensive discovery efforts have been directed at identification of synthetic-lethal target opportunities in *KRAS* mutant cancers. While

promising leads have been uncovered in some neoplastic settings, identification of chemically addressable targets robustly associated with *KRAS* mutation status has been a significant challenge. We considered that one obstacle to success may be phenotypic diversity among *KRAS* mutant cancers both between and within disease lineages. If this diversity is greater than or equivalent to commonality among *KRAS* mutant cancers, then primary chemical or genetic synthetic-lethal screening efforts using small collections of cell hosts would be subject to significant sampling bias. In light of this consideration, we defined *KRAS* mutation status within a panel of 106 non-small cell lung cancer-derived cell lines (*KRAS* mutant n=37, *KRAS* wild-type n=69)(Phelps et al., 1996; Shigematsu et al., 2005a; Shigematsu et al., 2005b; Yamamoto et al., 2008). Affinity propagation clustering (APC)(Frey and Dueck, 2007; Witkiewicz et al., 2015) was then used to delineate deterministic patterns of commonality, among these cell lines, derived from whole genome mRNA expression variation. At least 8 phenotypic clusters were recovered, and *KRAS* mutant lines were present within the majority of these clusters (Figure 3.1A). Moreover, the distribution of mRNA expression variation among all *KRAS* mutant cell lines was equivalent to that present among all other cell lines in the panel (Figure 3.1B). Together, these observations suggest the phenotypic diversity among *KRAS* mutant lung cancer cells is equivalent to the overall phenotypic diversity in the tested population. Therefore, in order to enrich for detection of bona fide synthetic-lethal genetic interactions with mutant *KRAS*, we selected 6 *KRAS* mutant and 6 *KRAS* wild-type cell lines, collectively distributed across the

phenotypic clusters, to serve as hosts for whole genome siRNA toxicity screens (Figure 3.1A; highlighted nodes). Two commercial libraries (4 (Dharmacon) or 3 (Ambion) siRNA duplexes per gene; one gene per well) were employed using an arrayed screening strategy with biological triplicates (Kim et al., 2013; Whitehurst et al., 2007). Batch and position corrected Z-scores were assigned to each siRNA pool according to cell viability measured 4 days post siRNA transfection. 7755 candidates were detected that reduced viability of at least one *KRAS* mutant line (Z score cutoff = -3, Figure 3.1C). To mitigate noise from “off-target” siRNA oligonucleotide sequence-specific effects and to account for the complexity of *KRAS*-independent phenotypic variation, we employed a two-class classifier (gene set enrichment analysis, GSEA) and score gene sets, rather than individual genes, which collectively selective activity in the *KRAS* mutant versus *KRAS* wild-type lines. Among 4725 curated mechanistic gene sets queried, 10 were identified as significantly enriched within the *KRAS* mutant cohort (Figure 3.2A; FDR<0.2, P<1e-16). Leading edge analysis indicated that multiple genes encoding nuclear transport machinery were in common among all the 10 gene sets (Figure 3.2B, C), and were responsible for selective enrichment of these sets in the *KRAS* mutant cohort (Figure 3.2D). This enrichment was also detectable by retrospective analysis of an independent shRNA viability screen in an isogenic pair of *KRAS* wild-type and *KRAS*<sup>G12D</sup> colorectal cancer cells (Luo et al., 2009) (Figure 3.2E). Among these components, chemical inhibitors have been designed against the nuclear export receptor XPO1. Therefore, selective sensitivity to XPO1 depletion was further examined across an additional 55 cell

lines and was found to be strongly correlated with *KRAS* mutation status (Figure 3.2F;  $P < 0.05$ ).

These observations nominated selective sensitivity to nuclear export activity for consideration as a mutant *KRAS*-associated vulnerability in lung cancer cells. To test this, we turned to the Selective Inhibitor of Nuclear Export (SINE) compounds, KPT-185 and KPT-330 (Selinexor)(Figure 3.3A). KPT-330 is currently being evaluated in humans against solid and hematologic tumors. These compounds covalently bind to the Cys528 of XPO1 to occlude a portion of the structural groove that otherwise accommodates nuclear export signal peptides on XPO1 cargo proteins; thereby inhibiting XPO1-dependent nuclear protein export in a dose-dependent manner. I selected 6 *KRAS* mutant and 6 *KRAS* wild-type cell lines and examined the effect of the compounds on cell viability. The test cohort of cell lines was selected with equivalent representation of cell proliferation rates among *KRAS* mutant and *KRAS* wild-type cells lines. This was done to avoid any confounding variables associated with the statistically significant enrichment of short doubling times we detected within the *KRAS* mutant cohort as a whole. ED50s for inhibition of cell viability following an 72 hour exposure ranged from 0.5  $\mu$ M to 10  $\mu$ M (Figure 3.3B), with significant selective dose sensitivity among the *KRAS* mutant cell lines compared to *KRAS* wild-type lines as indicated by area under the curve (AUC) with either compound (Figure 3.3C,D). Importantly, given the potentially broad-ranging consequences of nuclear export inhibition on cell biology, I found that selective sensitivity to XPO1 inhibition was independent of cell doubling time

variation (Figure 3.3E). I noted that among the *KRAS* mutant cell lines, A549 was an exception with respect to KPT-330 or KPT-185 sensitivity (Figure 3.3B,C,F-H). Therefore A549 was included in all subsequent analyses to represent potential mechanistic exceptions and/or contradictions to the *KRAS* synthetic-lethal hypothesis under investigation.

Selective sensitivity to XPO1 inhibitors was associated with remarkably selective induction of programmed cell death as indicated by caspase 3/7 activation (Figure 3.3F) and accumulation of cleaved PARP (Figure 3.3G). This offered the opportunity to test clearance of stationary-phase cell populations using doses equivalent to those achievable *in vivo* with the orally bioavailable XPO1 inhibitor KPT-330(Cheng et al., 2014). With the exception of A549, mutant *KRAS*-associated bimodal sensitivity to XPO1 inhibition was evident in this setting, with preservation of selectivity at doses over 400% higher than bioactive *in vivo* concentrations (Figure 3.3H). Notably, ectopic expression of oncogenic *KRAS* was sufficient to sensitize telomerase-immortalized non-tumorigenic lung epithelia (HBEC30) to XPO1 inhibitors in both proliferative and stationary-phase cultures (Figure 3.4A,B).

To validate target specificity of XPO1 inhibitors, cells were engineered to harbor mutation on the C528 using CRISPR/Cas9 genome editing. The cysteine residue is critical for XPO1-KPT compound interaction and was replaced with serine residue by CRISPR/Cas9-induced homologous recombination (Figure 3.5A)(Neggers et al., 2015). Remarkably, I observed that XPO1 C528S cells become resistant and no longer induce apoptosis in response to KPT-185 (Figure 3.5B,C).

I next evaluated conservation of efficacy and selectivity *in vivo* using three different mouse tumor models: subcutaneous xenograft tumor models with both *KRAS* wild-type and *KRAS* mutant NSCLC lines, *KRAS*<sup>G12D</sup> patient-derived xenograft (PDX) model and *Kras*<sup>LSL-G12V</sup>/*p53*<sup>fl/fl</sup> mouse model. As indicated above, KPT-330 is an orally available inhibitor with dose-proportional exposure in mice and humans. For the subcutaneous xenograft tumor models, animals were treated upon presentation of tumors of 100 mm<sup>3</sup> or larger with carrier, 3 mg/kg, or 10 mg/kg KPT-330 three times a week by oral gavage. This dosing schedule corresponds to average serum concentrations of 0.7 uM (3 mg/kg) and 2.0 uM (10 mg/kg). The *KRAS* wild-type line H2882 was not responsive to XPO1 inhibition, however excellent dose-dependent control of tumor burden over time was observed in the *KRAS* mutant lines H2009 and H460 (Figure 3.6A). For the PDX and GEM models, animals were stratified based on tumor burden, randomly assigned into two cohorts and treated with carrier or 10mg/kg KPT-330 using the same dosing schedule. KPT-330 significantly impaired growth of both the patient-derived *KRAS* mutant engrafted tumors and the spontaneous mouse lung tumors driven by oncogenic *Kras* (Figure 3.6B,D). Of note, 2 phenodeviant mice (outlier animals presenting with exceptionally high initial tumor burden) were subjected to a more aggressive dosing schedule (10mg/kg KPT-330 5 times a week) and showed remarkable tumor regression (Figure 3.5C).

To generate mechanistic leads that may account for selective addiction of *KRAS* mutant NSCLC cells to nuclear export, I first compared the whole genome transcript profiles of

XPO1 inhibitor-sensitive and resistant cell lines. GSEA identified NFκB target gene sets as enriched in the XPO1 inhibitor-sensitive cohort (Figure 3.7A,B), and NFκB target genes were highly overrepresented among the top 50 most differentially expressed genes in the sensitive versus resistant cohort (Figure 3.7C; Hypergeometric  $P < 1e-16$ ). NFκB signaling is often activated by oncogenic KRAS and can be crucial for oncogenic KRAS-driven tumor initiation and maintenance (Barbie et al., 2009; Basseres et al., 2014; Meylan et al., 2009). Of note, selective inhibition of XPO1 resulted in time-dependent nuclear accumulation of the NFκB negative regulatory protein IκB (Figure 3.7D), inhibition of NFκB transcriptional activity (Figure 3.7F) and inhibition of NFκB target gene expression (Figure 3.7E). The drug-resistant XPO1 allele cleanly reversed NFκB pathway sensitivity to KPT-185 (Figure 3.7F). I also employed whole-genome transcript array coupled to GSEA to evaluate the transcriptional change induced by XPO1 inhibition. GSEA returned NFκB target genes as the top gene sets down-regulated by KPT-185 (Figure 3.7G,H). In addition, *IκB* depletion was sufficient to confer XPO1 inhibitor resistance to otherwise sensitive *KRAS* mutant cells (Figure 3.8A-C). These observations suggest that *KRAS* mutant NSCLC cells require active nuclear export of IκB to maintain NFκB-dependent survival signaling. Consistent with this, ectopic expression of an IκB variant with an inactivated nuclear export signal sequence (NES) (Wuerzberger-Davis et al., 2011) was tolerated in *KRAS* wild-type but not *KRAS* mutant NSCLC cells (Figure 3.9A).

Notably, I found that the I $\kappa$ B kinase inhibitor BMS-345541 exhibited significant positive correlation with XPO1 inhibitor KPT-185, though with less potency and a narrower window of selectivity than observed with XPO1 inhibitors (Figure 3.9B,C). The latter is expected from the high biochemical IC<sub>50</sub> of BMS-345541 against IKK1 (IC<sub>50</sub>=4 $\mu$ M) and IKK2 (IC<sub>50</sub>=0.3 $\mu$ M)(Burke et al., 2003). I observed XPO1 inhibition-induced nuclear accumulation of I $\kappa$ B in all cell lines tested (Figure 3.9D), indicating that selective sensitivity to these compounds is likely due to context-specific consequences of inhibition of NF $\kappa$ B signaling rather than variability of target inhibition. Consistent with this, I found that KPT-330 resistant tumors displayed extensive nuclear accumulation of I $\kappa$ B in response to KPT-330 exposure *in vivo* (Figure 3.9E). Together, these observations indicate that oncogenic KRAS induces XPO1-dependent activation of NF $\kappa$ B signaling in NSCLC cells to support cell survival, but that NF $\kappa$ B pathway activation is not generally required in NSCLC tumor lines with KRAS-independent mechanistic etiologies.

From independent pan-cancer cell line screening efforts, the *KRAS* mutant NSCLC cell lines H2030 and H2122 were identified as poor responders to XPO1 inhibitors (Karyopharm Therapeutics personal communication); which was validated with 9-point dose response analyses (Figure 3.10A). We leveraged this finding to address potential mechanisms of KPT-330 resistance in *KRAS* mutant NSCLC. From whole exome sequence data, biclustering was used for empirical discovery of gene-level non-synonymous somatic alterations selectively co-occurring with XPO1 resistance status in *KRAS* mutant NSCLC.

lines. Somatic nucleotide variants of *FSTL5* (Follistatin-like 5) were the sole correlate identified (Figure 3.10B,C). Two previously untested *KRAS* mutant cell lines with co-occurring *FSTL5* mutations, H2291 and H1573, were available in the NSCLC panel. Both lines were found to be robustly resistant to XPO1 inhibitors relative to *KRAS* mutant NSCLC cell lines with wild-type *FSTL5* (Figure 3.10C,D). Somatic mutations in *FSTL5* were detected in 10% of lung adenocarcinomas by TCGA, with an allele distribution reminiscent of loss-of-function alterations (Figure 3.12F). Though poorly understood at molecular resolution, *FSTL5* has been nominated as a tumor suppressor protein in hepatocellular cancer (HCC)(Zender et al., 2008; Zhang et al., 2015). Notably, *in vivo* RNAi screens of genes found to be focally deleted in HCC identified *Fstl5* depletion among the top three perturbations, observed with multiple shRNAs, that cooperated with Myc to induce HCC in mice (Figure 3.11E)(Zender et al., 2008)

I found that *FSTL5* depletion had no detectable consequence in *FSTL5* mutant NSCLC lines, however, sensitivity to XPO1 inhibitors was significantly reduced upon depletion of *FSTL5* in *KRAS* mutant, *FSTL5* wild-type NSCLC lines (Figure 3.11A-C). Furthermore, ectopic *FSTL5* expression was tolerated in *FSTL5* wild-type but not *FSTL5* mutant cell lines (Figure 3.11D); suggesting that *FSTL5* inactivation is under selective pressure in some cancer genomes. Together, these observations suggest the *FSTL5* mutations detected in cancer cells are loss-of-function and promote resistance to XPO1 inhibition.

Defective YAP signaling is a major etiological factor for development of HCC, and YAP inactivation is sufficient to induce regression of advanced HCC in mouse models of disease (Fitamant et al., 2015). This, together with the emerging paradigm of YAP-dependent acquired resistance to *Kras* ablation in mouse lung and pancreas cancers and targeted therapy resistance in melanoma (Kapoor et al., 2014; Lin et al., 2015a; Shao et al., 2014a), lead us to evaluate the consequence of *FSTL5* loss on YAP activity. We found that human lung adenocarcinomas (TCGA LUAD, n=181) harboring *FSTL5* somatic alterations displayed significant enrichment of YAP1 protein expression as compared to *FSTL5* wild-type tumors (Figure 3.12A). Notably, *FSTL5* depletion by siRNA in *KRAS* mutant *FSTL5* wild-type cells was sufficient to induce YAP1 protein stabilization (Figure 3.12B). Four independent siRNA oligonucleotides show exquisite correlation of target knockdown to phenotype (Figure 3.12C). Furthermore, whole-genome transcript profiling revealed that the *FSTL5*-dependent gene expression program was significantly enriched with genes also induced upon depletion of *LATS1* and *LATS2* tumor suppressors (Figure 3.12F; Hypergeometric  $P < 1e-16$ ). To evaluate this relationship in patient samples, 37 *KRAS* mutant lung adenocarcinoma specimens were immunostained for characterization of YAP1 protein accumulation and localization. The resulting slides were scored by experienced lung cancer pathologists, blinded to the study objectives, for percent of YAP1 positive tumor cell nuclei, and relative YAP1 nuclear/cytoplasmic distribution. Comparison to H2009 (*KRAS* mutant, *FSTL5* wild-type) and H2030 (*KRAS* mutant, *FSTL5* mutant) cell blocks revealed 3 outlier tumors (1805,

1930, and 2279) with predicted YAP pathway activation (Figure 3.12D). Sanger sequencing of *FSTL5* exons in all three identified 2 samples harboring somatic non-synonymous *FSTL5* alterations (Figure 3.12D,E). These observations indicate a strong and clinically relevant association between *FSTL5* mutation status and YAP1 protein accumulation that is consistent with Hippo tumor suppressor pathway inactivation.

Importantly, I observed that direct activation of YAP1 via depletion of the *LATS1/2* tumor suppressors and exogenous YAP1 overexpression was sufficient to confer resistance to XPO1 inhibition in otherwise sensitive *KRAS* mutant NSCLC cells (Figure 3.13A-F). Furthermore, chemical (AICAR) or genetic (siYAP/TEAD2) inhibition of YAP1 transcription factor activity was sufficient to confer XPO1 inhibitor sensitivity to otherwise resistant *KRAS* mutant NSCLC cells (Figure 3.13G-J). AICAR-induced AMPK activation can inhibit productive YAP1/TEAD interactions by phosphorylation of YAP1 S94 (Mo et al., 2015). I found that AICAR reversed resistance to XPO1 inhibition, but only in *KRAS* mutant cell lines with an intact AMPK response (Figure 3.13G-I, K). Thus *FSTL5* is mechanistically coupled to YAP1 pathway activation and thereby specifies sensitivity of *KRAS* mutant NSCLC cells to chemical inhibition of XPO1.

Evaluation of the sensitivity of an additional 13 NSCLC lines (6 *KRAS* wild-type and 7 *KRAS* mutant) to XPO1 inhibition identified one unexpected *KRAS* wild-type responder (H1648) and two unexpected *KRAS* mutant non-responders (HCC515, Calu1) (Figure 3.14A). Of note, we found that H1648 harbors genomic amplification of *IKK $\beta$*  together with

a transcript profile indicative of NF $\kappa$ B pathway activation (Figure 3.14B), suggesting sensitivity to XPO1 inhibition due to KRAS-independent addiction to NF $\kappa$ B signaling. On the other end, HCC515 and Calu1 were found to harbor LATS1 mutation (LATS1 R904\*) and loss of Merlin expression (Figure 3.14D), respectively. Both responded to YAP1 inhibition in combination with KPT-330 (Figure 3.14C). Thus, these additional “exceptions to the rule” were accounted for within the mechanistic context of the study as a whole.

**Figure 3. 1**

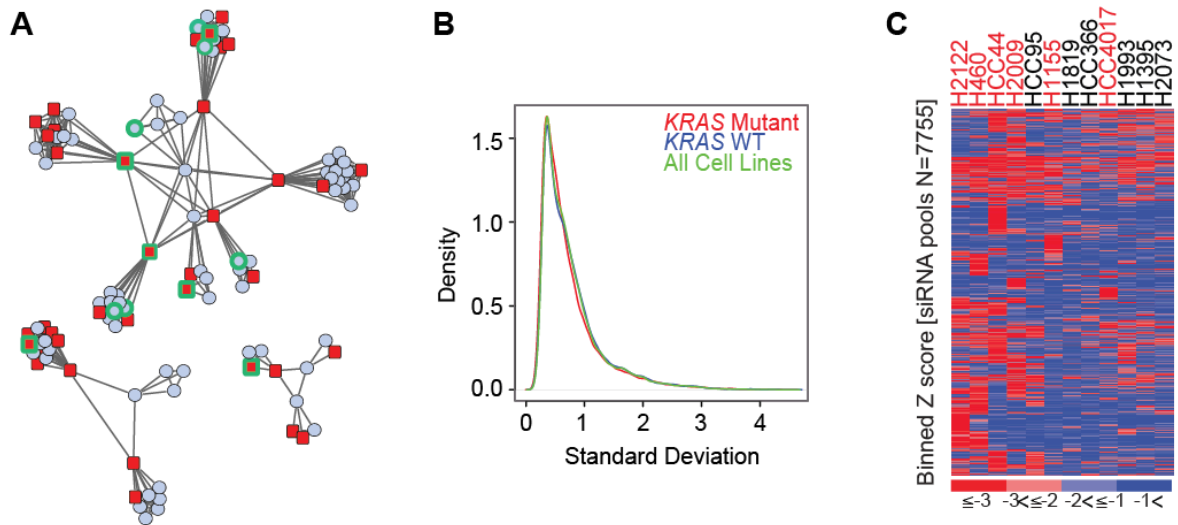


**Figure 3.1. Phenotypic diversity among *KRAS* mutant NSCLC lines**

(A) Affinity propagation-based similarity clusters of NSCLC lines based on whole genome mRNA expression variation. Two-dimensional projection of the three-dimensional clustering result is shown. The nodes represent cell lines and the edges represent Euclidean distance between cell lines as determined by gene expression variation. Red nodes: *KRAS* mutant (n=37), Blue nodes: *KRAS* WT (n=69). 12 NSCLC cell lines subjected to whole genome siRNA toxicity screening are highlighted in green. (B) Distribution of mRNA expression variation among *KRAS* mutant lines (red curve, n=37), *KRAS* WT lines (blue curve, n=69) and all NSCLC lines (green curve). (C) Binned Z-score distributions of selectively toxic gene depletions across the indicated cell lines. Cell lines (columns; red label=*KRAS* mutant, black label=*KRAS* WT) and siRNA target genes (rows) are clustered by 2-way unsupervised UPGMA.

### Figure 3. 2

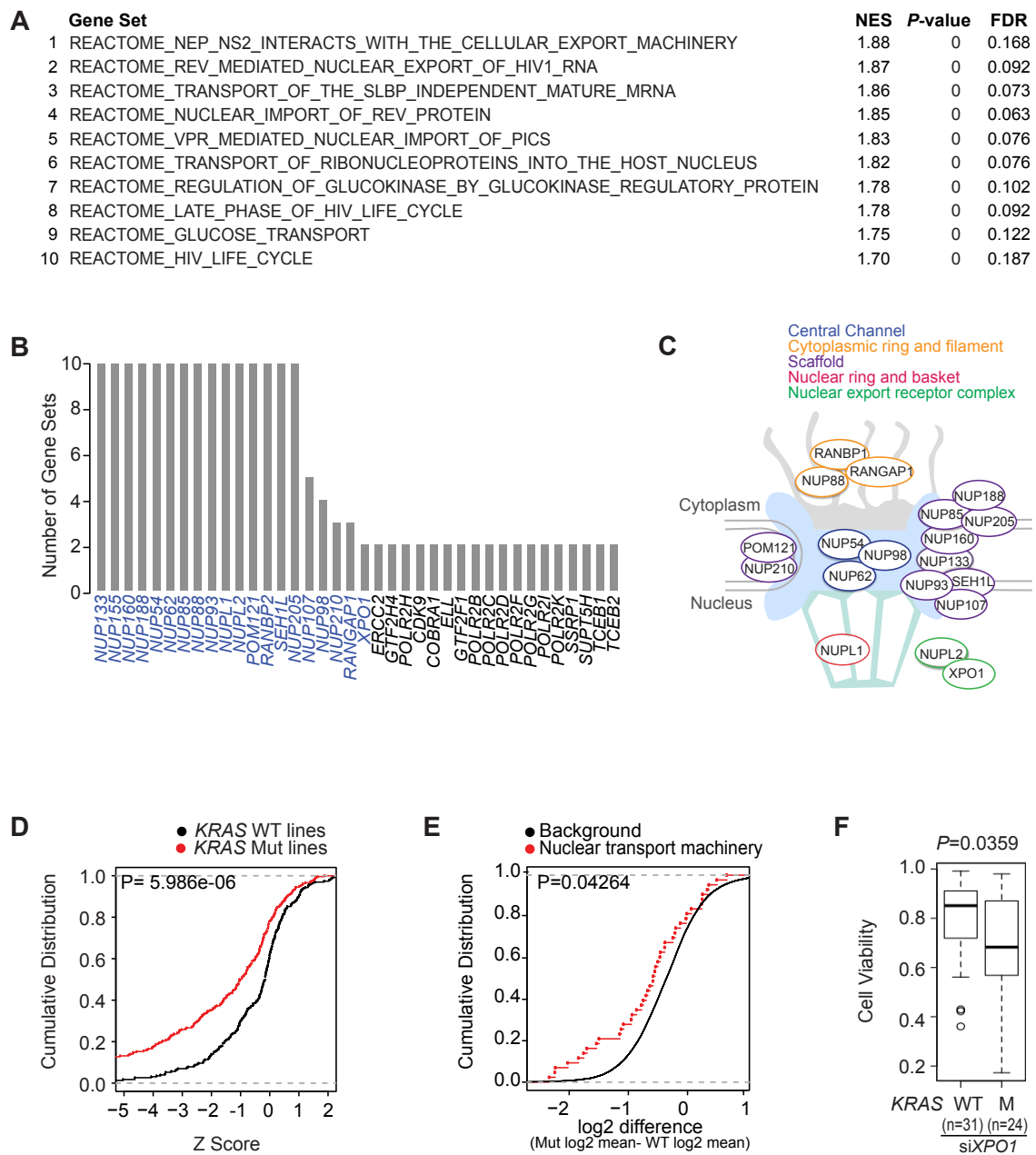


**Figure 3.2. Synthetic-lethal genetic interactions in *KRAS* mutant NSCLC cells.**

(A) Top-ranked gene sets ( $\text{FDR} < 0.2$ ,  $P < 1\text{e-}16$ ) returned by functional GSEA. (B) Leading edge gene representation among the gene sets in (A). Known components of nuclear transport machinery (indicated in (C)) are labeled in blue. (C) Biological process representation of the leading-edge synthetic-lethal gene depletion targets. (D) Cumulative distributions of the viability Z-scores for siRNA pools, targeting genes in (C), among *KRAS* mutant versus *KRAS* WT cell lines. KS test  $P$  value is indicated. (E) Cumulative distributions of log2 difference scores for depletion of shRNAs in *KRAS* mutant versus *KRAS* wild-type cells. Red: shRNAs targeting genes encoding nuclear transport machinery from (C). Black: all other shRNAs. KS test  $P$  value is indicated. Data is from Ji Luo et al. (2009). (F) Differential cell viability following *XPO1* depletion in *KRAS* mutant cell lines versus *KRAS* WT cell lines. Boxplots indicate median and interquartile range (IQR). Unpaired t-test was used for the comparison.

**Figure 3. 3**

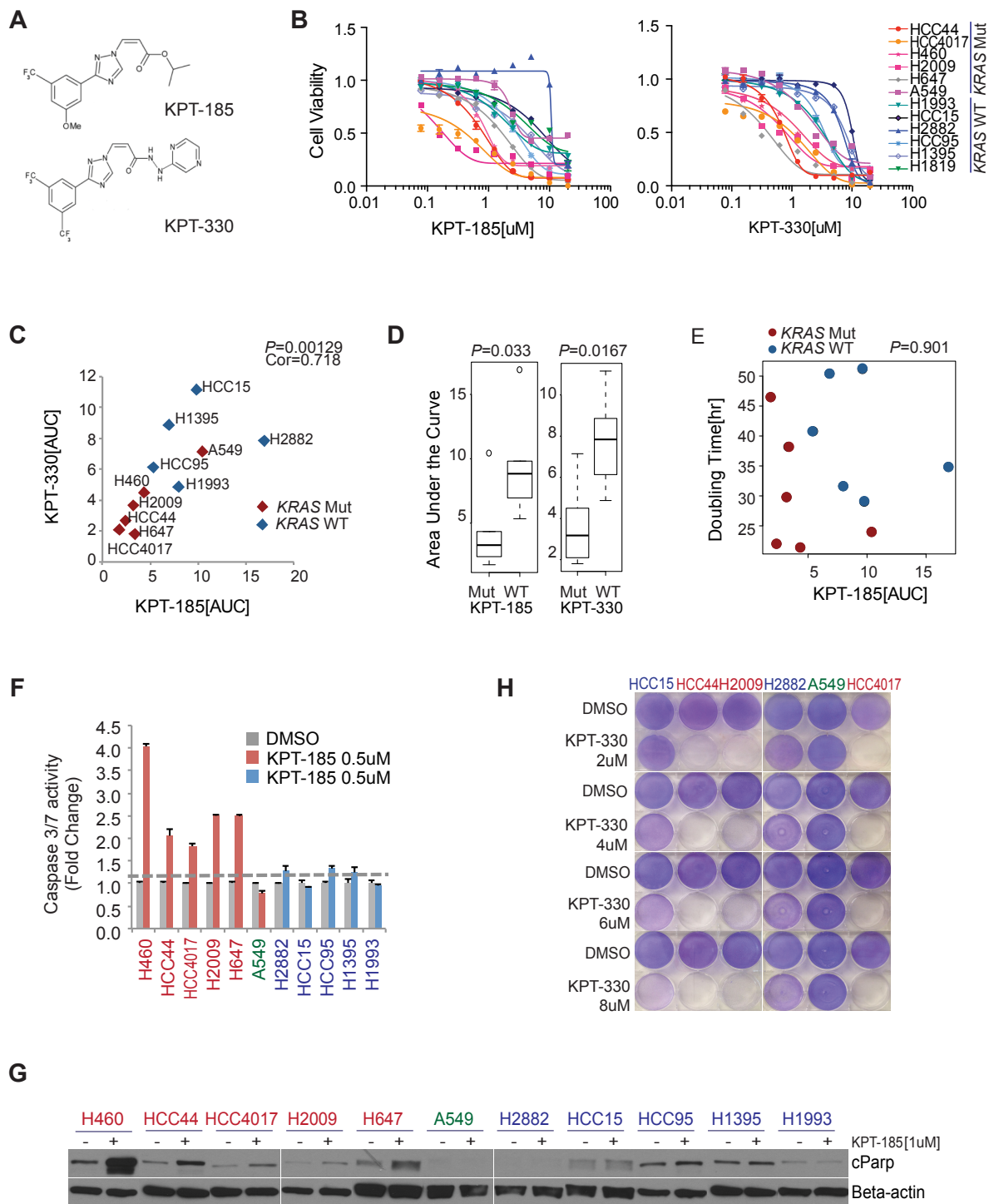


**Figure 3.3. Selective sensitivity of *KRAS* mutant NSCLC cells to chemical inhibition of the nuclear transport receptor XPO1.**

(A) Structures of SINE compounds (XPO1i), KPT-185 and KPT-330. (B) Dose-response viability curves for the indicated panel of NSCLC lines following a 72-hour exposure to KPT-330. Mean of triplicates  $\pm$  standard deviation (s.d.) is shown. (C) Correlation of sensitivity to the XPO1 inhibitors KPT-330 and KPT-185 as indicated by Area Under the dose-response Curves (AUCs) from (B). Red: *KRAS* mutant, Blue: *KRAS* WT. Pearson correlation *P* value is indicated. (D) Significant differential response of *KRAS* mutant and *KRAS* WT NSCLC cell cohorts to the indicated XPO1 inhibitors. Boxplots indicate median and IQR. Unpaired t-test was used for the comparisons. (E) Scatter plot of cell line doubling time versus KPT-185 sensitivity. Pearson correlation *P* value is indicated. (F) Selective induction of caspase 3/7 activity in *KRAS* mutant lines following a 24-hour exposure to 0.5uM KPT-185. Red: *KRAS* mutant/sensitive, Green: *KRAS* mutant/resistant, Blue: *KRAS* WT. Bars indicate mean of duplicates + s.d. (G) Selective time-dependent accumulation of cleaved PARP in *KRAS* mutant lines following exposure to 1uM KPT-185. Labels as in (F). Beta-actin is shown as a loading control. (H) Cytotoxic effects of KPT-330 on stationary-phase cell populations following a 5-day exposure to the indicated concentration of KPT-330 (6-day exposure for 2uM KPT-330). Resulting monolayers, stained with crystal violet, are shown.

**Figure 3. 4**

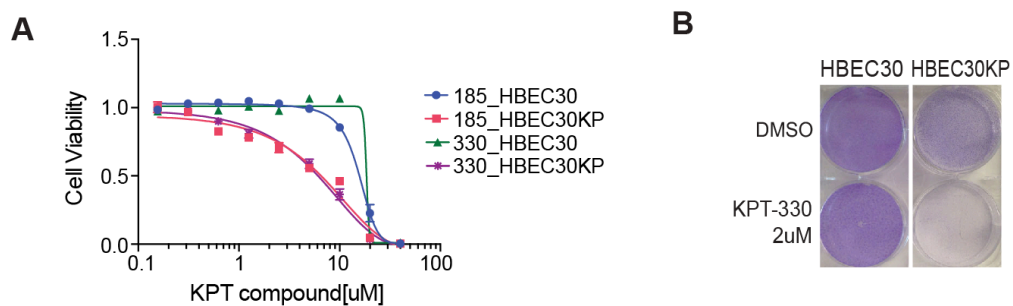


**Figure 3.4. Ectopic expression of oncogenic KRAS is sufficient to sensitize normal lung epithelia to XPO1 inhibitor.**

(A) Selective response of oncogenic KRAS<sup>G12V</sup> expressing lung epithelia (HBEC30KP), versus KRAS WT parental epithelia (HBEC30), to KPT-185 and KPT-330. Mean of triplicates  $\pm$  s.d. is shown. (B) Cytotoxic effects of 2uM KPT-330 on stationary-phase cell populations following a 6-day exposure to KPT-330.

Figure 3. 5

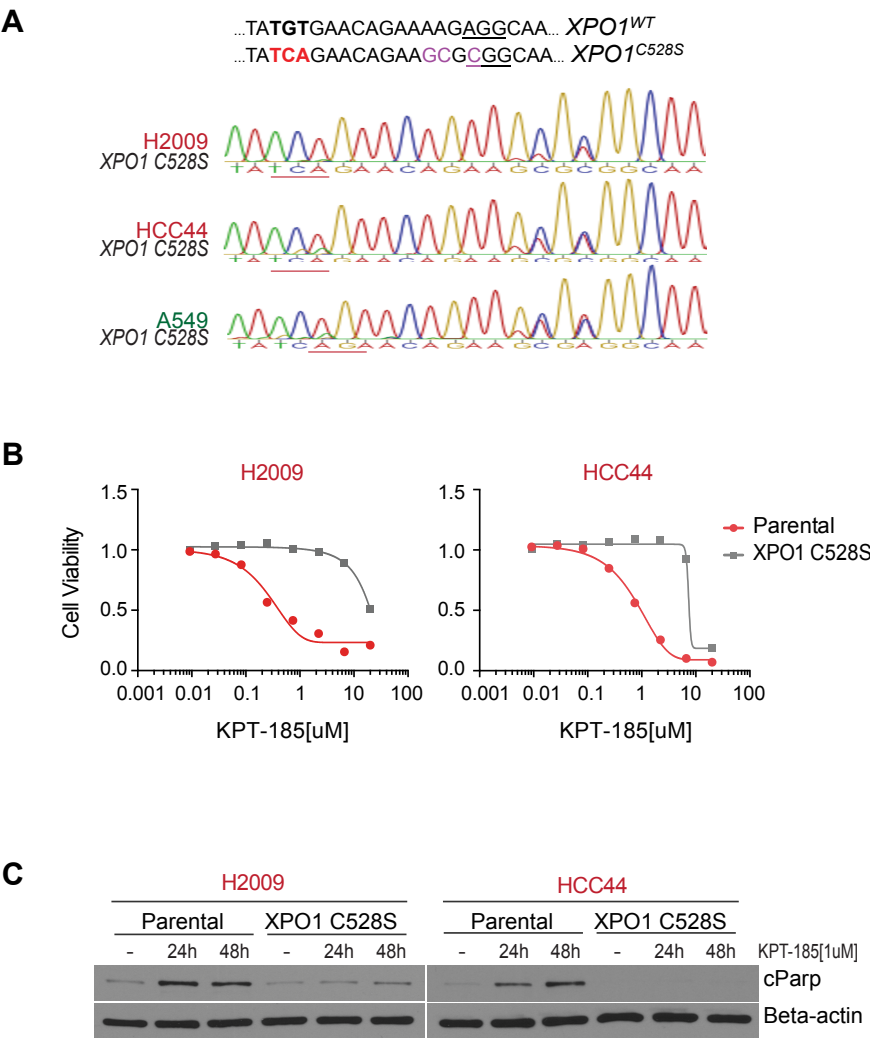


**Figure 3.5. Validation of target-specificity of XPO1 inhibitor.**

(A) Sequencing chromatogram of *XPO1* genomic DNA of genome edited cells. TGT (cysteine 528 residue) was replaced with TCA (serine residue) by CRISPR/Cas9-induced homologous recombination. Three synonymous mutations were simultaneously introduced near the PAM site in order to prevent re-cutting of the recombined DNA. (B) Rescue of XPO1 inhibitor toxicity by gene editing. Dose-response curves are as in Figure 3.3B. (C) Rescue of apoptotic response to XPO1 inhibition by gene editing. Immunoblots are as in Figure 3.3G.

**Figure 3. 6**

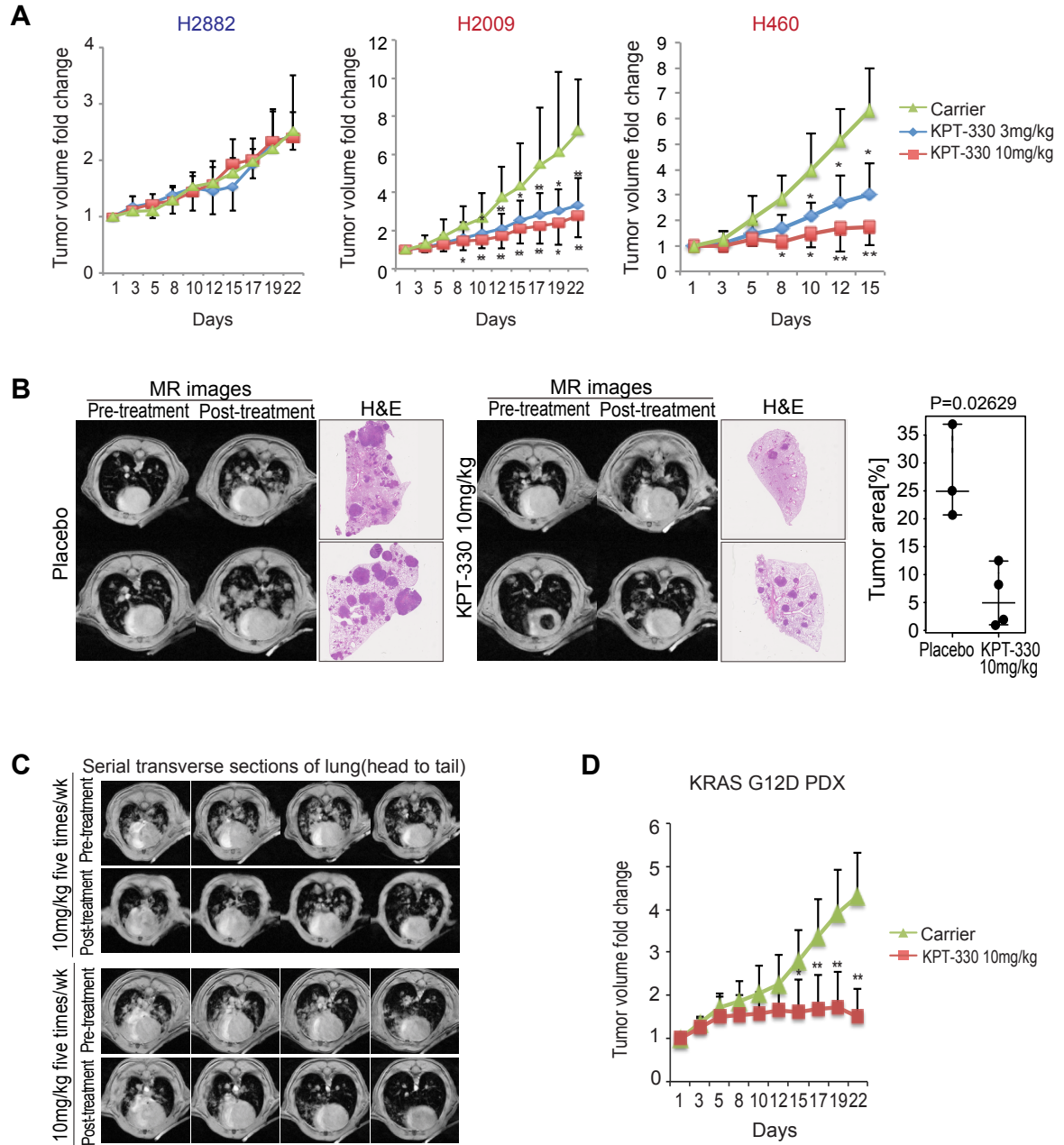


**Figure 3.6. Efficacy and selectivity of KPT-330 *in vivo*.**

(A) Tumor volume fold change during XPO1 inhibition in *KRAS* WT (H2882) or *KRAS* mutant (H2009 and H460) NSCLC cells. \*  $P < 0.05$ , \*\*  $P < 0.01$ , Unpaired t-test, mean and standard deviation. (B) Representative lung MR image of *Kras*<sup>LSL-G12D</sup>/*P53*<sup>fl/f</sup> mouse is shown before and after treatment for each cohort. Post-treatment H&E-stained left lung lobe is shown. Tumor burden was calculated as the tumor area divided by lung area. Unpaired t-test was used for the comparisons. (C) Lung tumor burden pre- and post-treatment as indicated by MR images. 2 mice presenting with exceptionally high initial tumor burden were treated with 10mg/kg KPT-330 5 times per week. Lungs were imaged with serial transverse MR sections on treatment day 0 and again on treatment day 21. (D) Tumor volume fold change of patient-derived *KRAS*<sup>G12D</sup> mutant lung adenocarcinoma xenografts during XPO1 inhibition. \*  $P < 0.05$ , \*\*  $P < 0.01$ , Unpaired t-test, mean and standard deviation.

**Figure 3. 7**

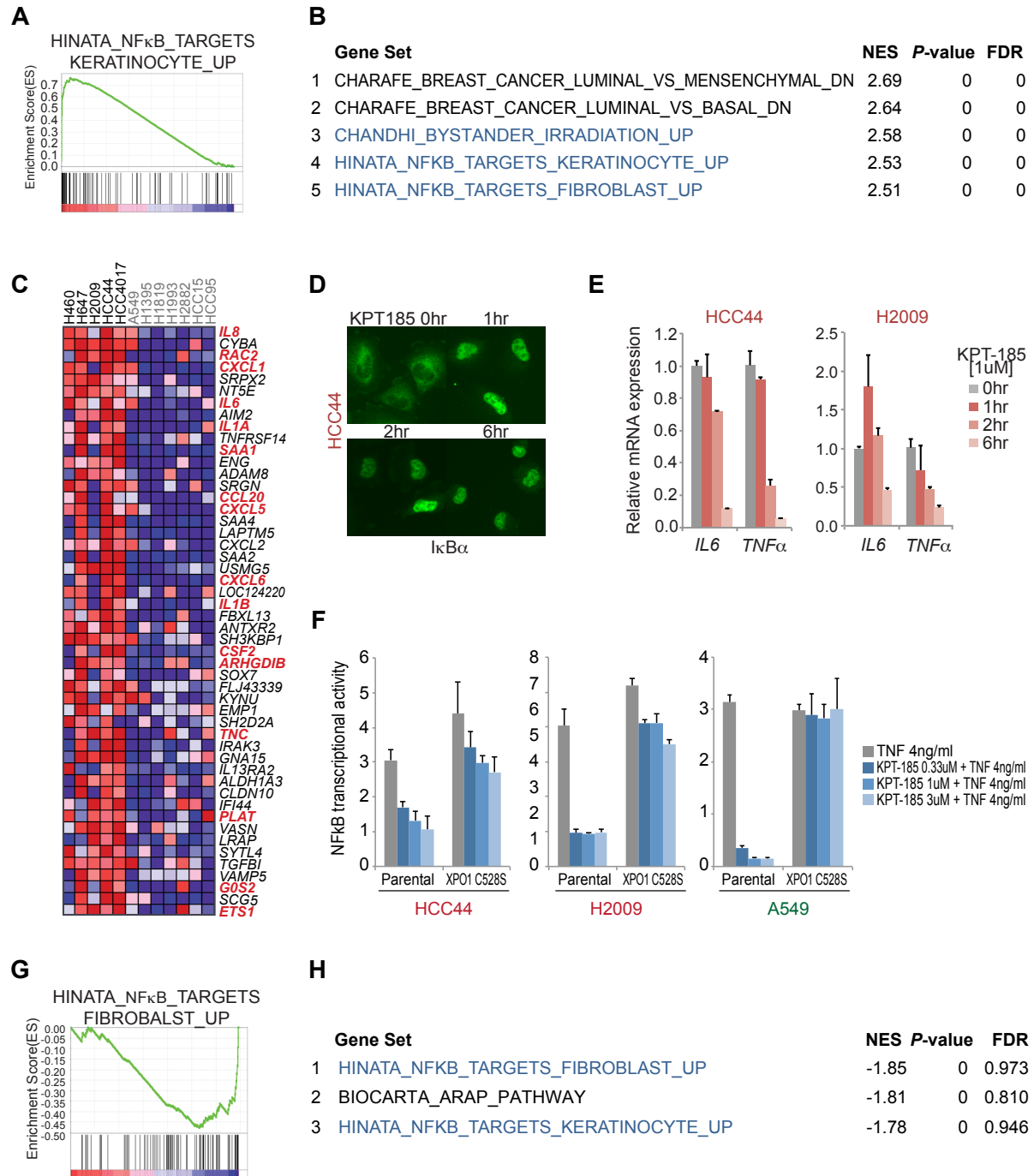


**Figure 3.7. Selective addiction to NFκB activity specifies sensitivity to XPO1 inhibitor.**

(A) NFκB transcriptional target enrichment plot (XPO1i-sensitive versus XPO1i-resistant). (B) Top 5 gene sets that significantly discriminate XPO1i-sensitive lines from XPO1i-resistant lines. NFκB target gene sets are indicated in blue. (C) Top 50 differentially expressed genes ranked by signal-to-noise (S2N) ratio between XPO1i-sensitive versus XPO1i-resistant cohort. Known NFκB targets are indicated in red (16/133; Hypergeometric  $P < 1e-16$ ). (D) Time-dependent nuclear accumulation of IκBα in response to 1μM KPT-185. (E) Time-dependent inhibition of NFκB target gene expression in response to 1μM KPT-185. Bars indicate mean of triplicates + s.d. (F) Rescue of NFκB transcriptional activity by gene editing. Luminescence-based NFκB reporter activity is shown. Cells were exposed to the indicated compounds for 24hrs followed by 4ng/ml TNFα for 4hrs. Luminescence signals were normalized to control luminescence signals and then normalized to DMSO only control. Bars indicate mean of triplicates + s.d. (G) Enrichment plot of NFκB target genes (KPT-185 - treated versus DMSO -treated). (H) Top 3 gene sets that are downregulated by a 12-hour exposure to XPO1 inhibitor. NFκB target gene sets are indicated in blue.

**Figure 3. 8**

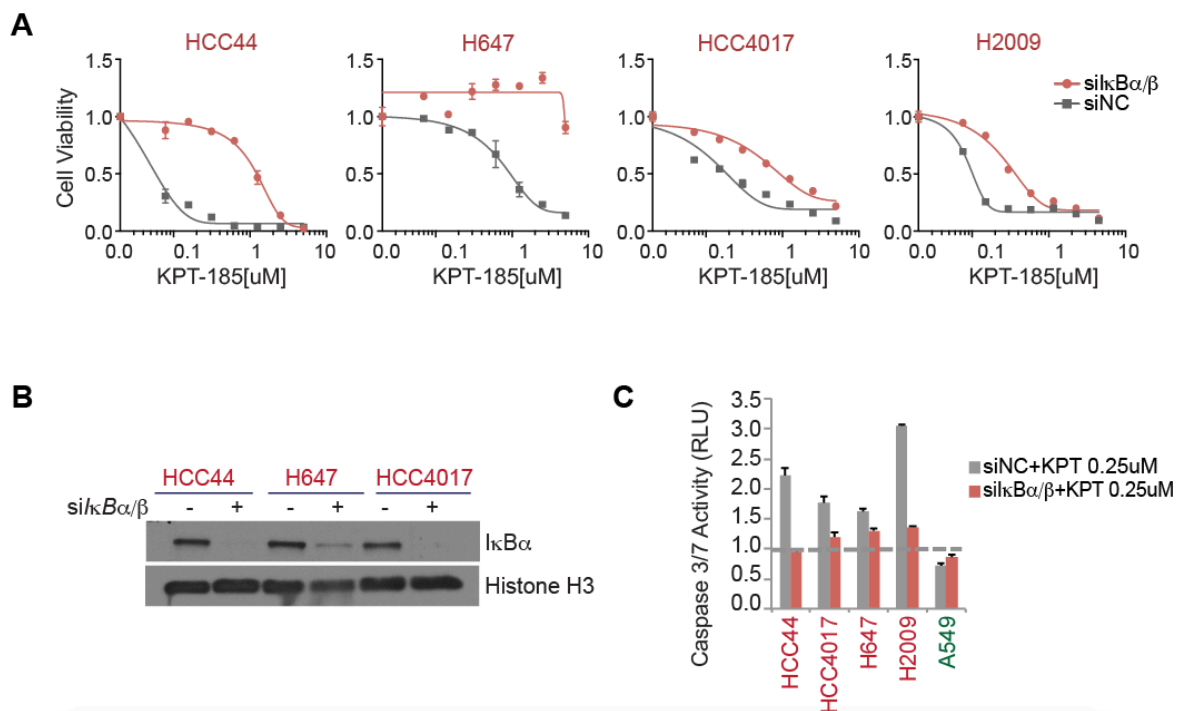


**Figure 3.8.  $\kappa$ B depletion is sufficient to confer XPO1 inhibitor resistance to *KRAS* mutant NSCLC cells.**

(A)  $\kappa$ B-dependent sensitivity to KPT-185. 24hr post-transfection with the indicated siRNAs, cells were exposed to the indicated concentrations of XPO1i for 72 hours. Mean of duplicates  $\pm$  s.d. is shown. (B) Immunoblot of  $\kappa$ B $\alpha$  48hr post-transfection of si $\kappa$ B $\alpha/\beta$  for confirmation of target depletion. Histone H3 is shown as a loading control. (C)  $\kappa$ B-dependent induction of apoptosis by XPO1i. Cells treated as in (A) were exposed to 0.25uM KPT-185 for 48 hours. Bars indicate mean of triplicates  $\pm$  s.d.

**Figure 3.9**

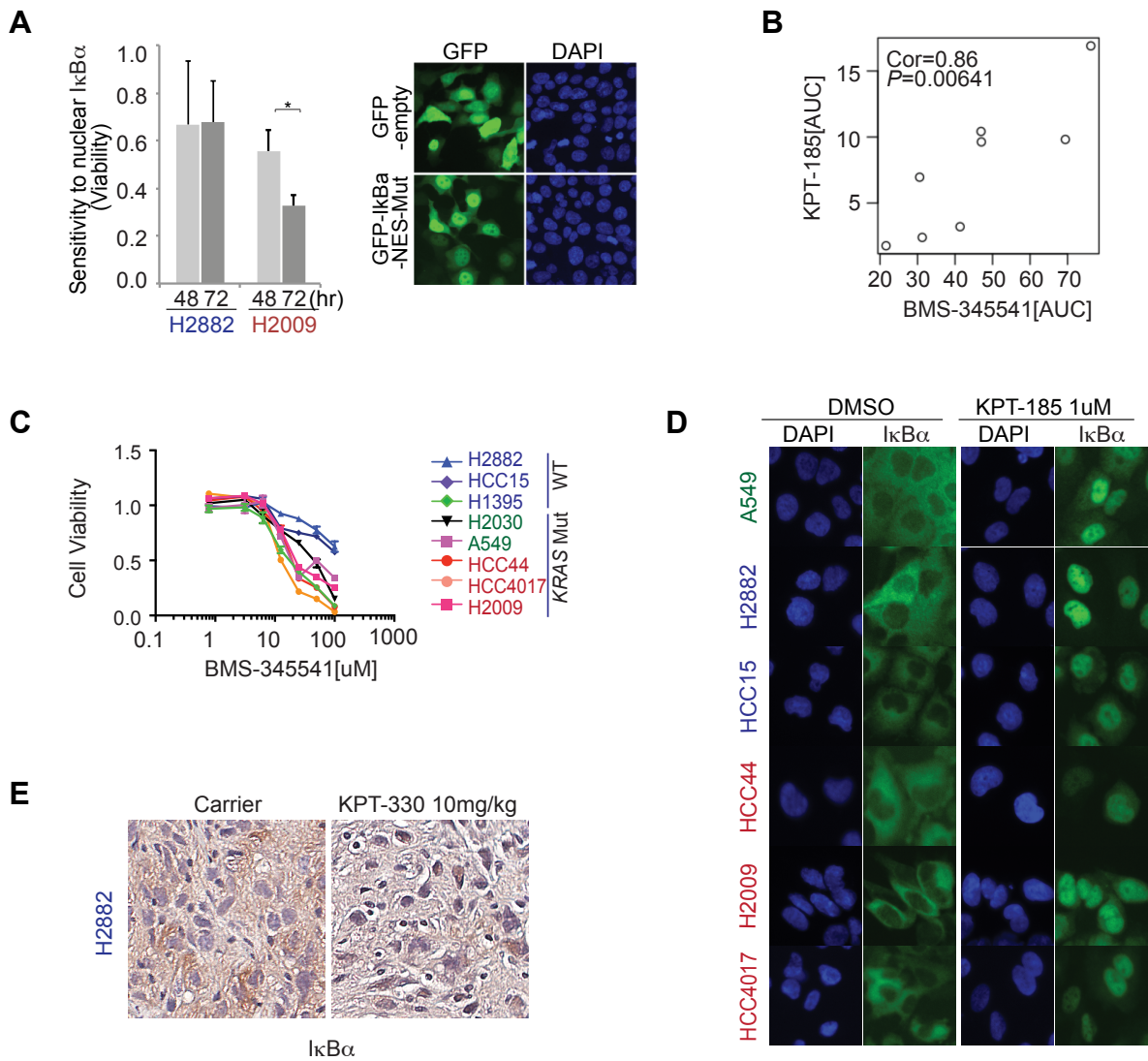


**Figure 3.9. Selective sensitivity to XPO1 inhibition is likely due to context-specific consequences of inhibition of NFκB signaling.**

(A) Intolerance to ectopic nuclear accumulation of IκBα in XPO1i-sensitive cells. Left: Y-axis indicates fold change in % of GFP positive nuclei of GFP-IκB-NES-mutant positive cells normalized to GFP-empty vector positive cells. Bars indicate mean + s.d of three independent experiments (\*  $P < 0.05$ , Unpaired t-test). Right: 293T cells transfected with the indicated plasmids to confirm plasmid transfection efficiency and localization of ectopically expressed proteins. Cells were fixed and photographed 48hr post-transfection. (B) Positive correlation between sensitivity to KPT-185 and BMS-345541 ( $P < 0.01$ , Pearson correlation). AUCs determined from Figure 3.3B and 3.9C. (C) Dose-response curves of a panel of NSCLC lines following a 72-hour exposure to BMS-345541. Red labels: *KRAS* mutant/XPO1i-sensitive, Green labels: *KRAS* mutant/XPO1i-resistant, Blue labels: *KRAS* WT. Mean of duplicates +/- s.d. is shown. (D) Subcellular localization of IκBα in the presence of 1μM KPT-185. Cells were exposed to KPT-185 for 24hrs. Label colors as in (C). (E) Nuclear accumulation of IκBα in xenograft tumors in response to KPT-330 *in vivo*.

**Figure 3.10**

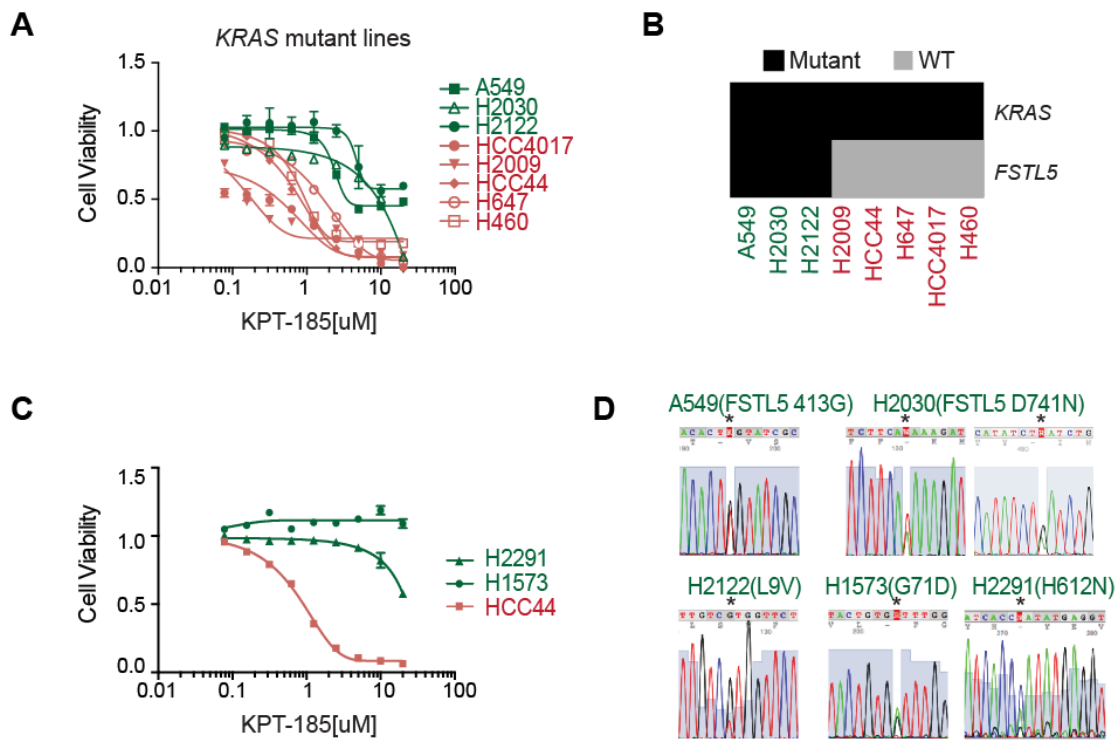


**Figure 3.10. Co-occurring mutations in *FSTL5* are associated with intrinsic resistance of *KRAS* mutant lines to XPO1 inhibitor.**

(A) Dose-response viability curves for H2122 and H2030 following a 72-hour exposure to KPT-185. Mean of triplicates  $\pm$  s.d. is shown. Data is overlaid with responses of the indicated lines from Figure 3.3B for comparison. (B) Biclustering identifies somatic *FSTL5* variants associated with XPO1i-resistance. Red labels: *KRAS* mutant/XPO1i-sensitive, Green labels: *KRAS* mutant/XPO1i-resistant. (C) KPT-185 dose-response curves of predicted XPO1i-resistant lines (H2291 and H1573) based on *KRAS* and *FSTL5* mutation status. Mean of triplicates  $\pm$  s.d. is shown. (D) Sanger-sequencing chromatograms of detected *FSTL5* variants in the indicated cell lines.

**Figure 3. 11**

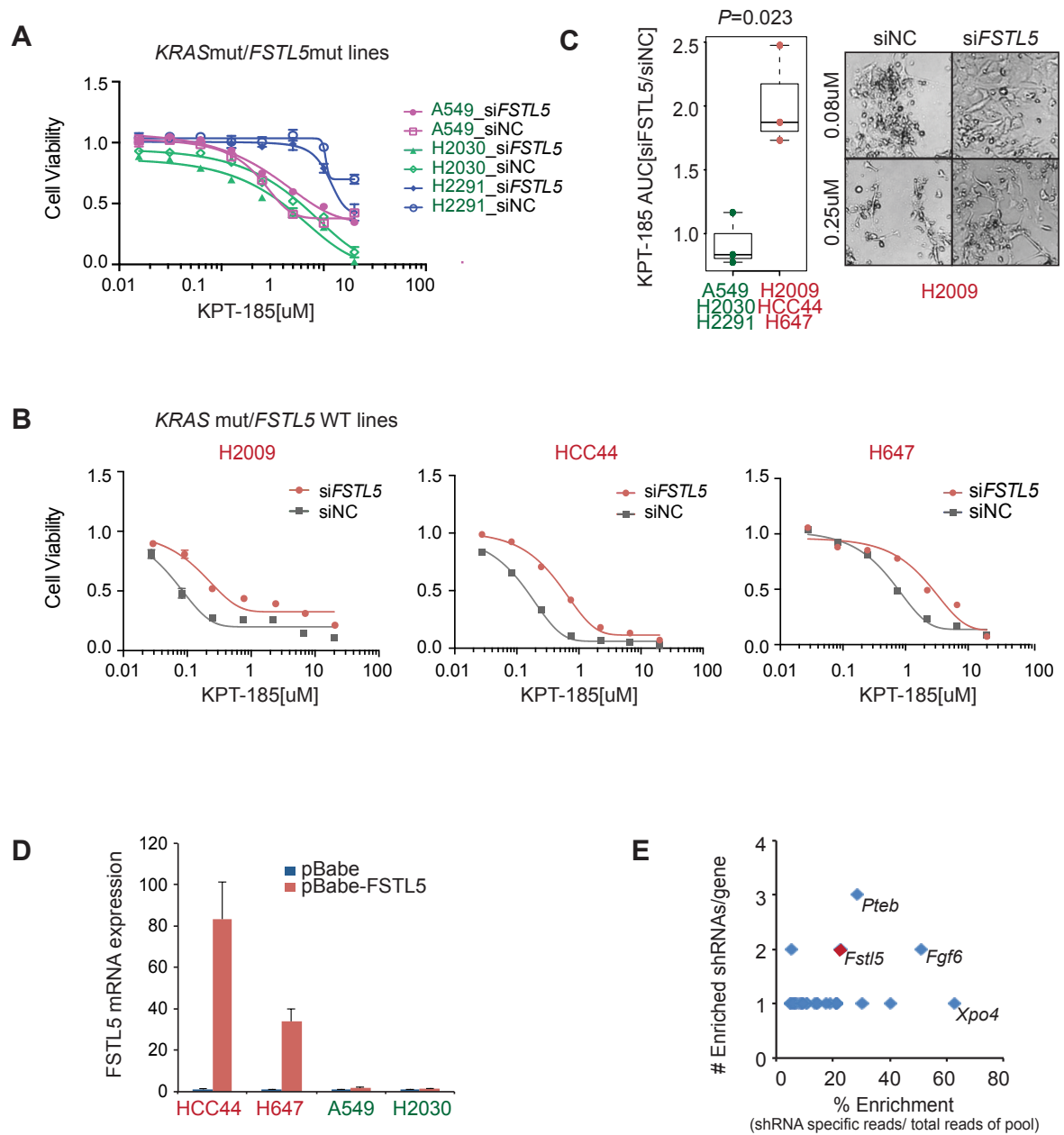


**Figure 3.11. *FSTL5* mutations detected in cancer cells are loss-of-function mutations and promote resistance to XPO1 inhibitor.**

(A,B) KPT-185 dose response of cells transfected with the indicated siRNAs as in Figure 3.8A. Panel A: *KRAS* mutant /*FSTL5* mutant lines. Panel B: *KRAS* mutant/*FSTL5* WT lines. Mean of duplicates +/- s.d. is shown. (C) Selective effects of *FSTL5* depletion on the XPO1i-sensitivity of *KRAS* mutant/*FSTL5* wild-type lines (red) versus *KRAS* mutant/*FSTL5* mutant lines (green). Box plot indicates fold changes in AUC of si*FSTL5*-transfected cells normalized to siNC-transfected cells. AUCs calculated from (A) and (B). Representative cell culture images are shown on the right. (D) Relative ectopic expression of *FSTL5* mRNA. Cells were infected with retrovirus carrying the indicated plasmids. Following a 7-day puromycin selection, cells were harvested for quantitative RT-PCR. (E) Tumor suppressor genes identified in oncogenomics-based *in vivo* RNAi screen(Zender et al., 2008). Among the genes targeted by 36 shRNAs overrepresented during HCC tumor development, *Fstl5* was the third ranked gene suppressed by >1 enriched shRNA. X-axis indicates number of shRNAs per gene among the 36 enriched shRNAs. Y-axis indicates shRNA specific reads over a total 2307 sequence reads.

Figure 3. 12

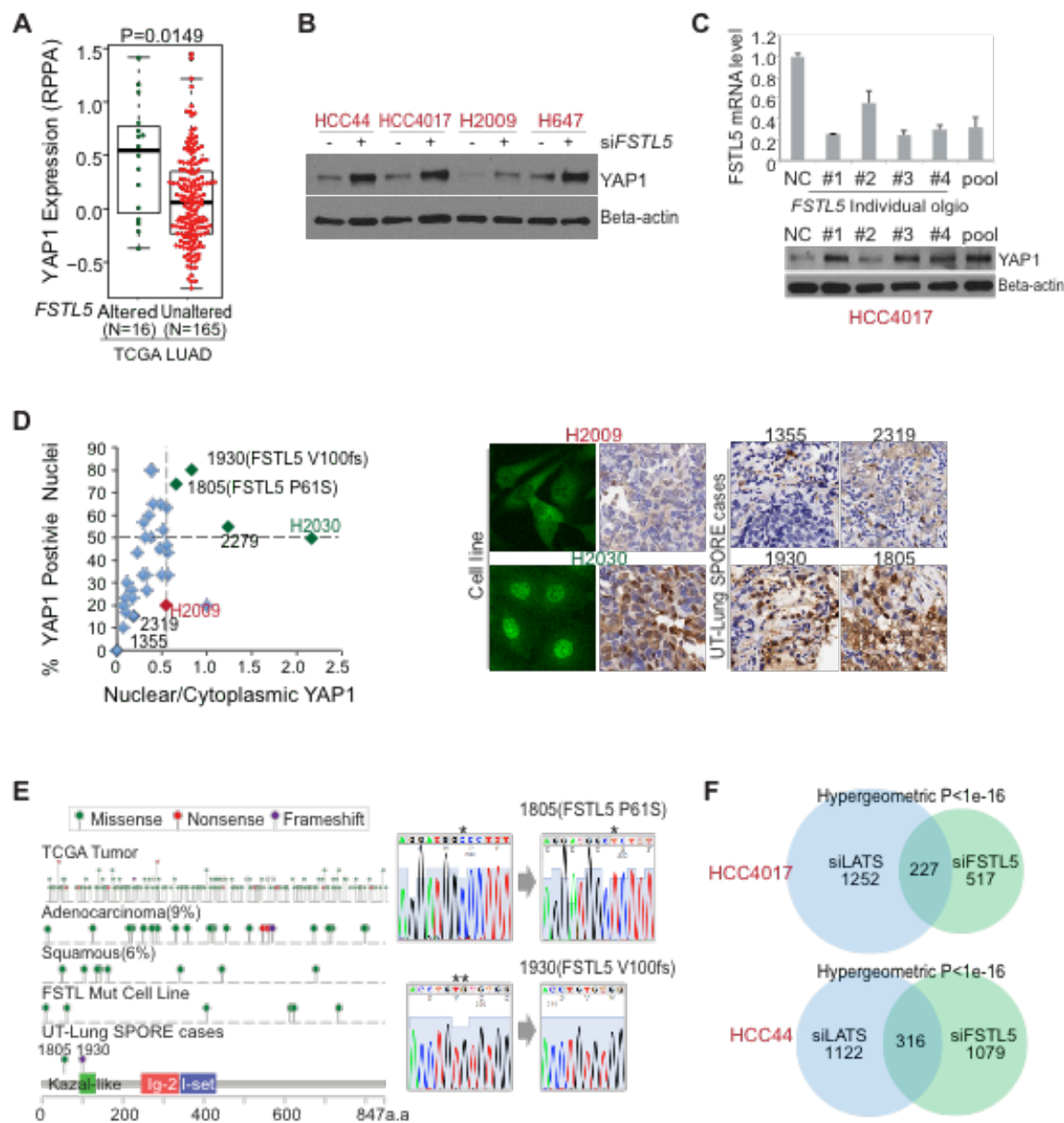


**Figure 3.12. Association between *FSTL5* mutation status and YAP1 protein accumulation.**

(A) Significant enrichment of YAP1 protein expression in tumors harboring *FSTL5* somatic alterations as compared to *FSTL5* wild-type tumors (TCGA LUAD). Unpaired t-test was used for the comparison. (B) YAP1 protein accumulation 72hr post-transfection with *FSTL5* siRNAs. (C) Expression of *FSTL5* mRNA(upper panel) and YAP1 protein(bottom panel) following transfection with the indicated siRNAs targeting *FSTL5*. 72hr post-transfection, cells were collected for parallel RT-PCR and immunoblotting. (D) Relative nuclear/cytoplasmic YAP1 distribution and % YAP1 positive nuclei in *KRAS* mutant lung tumors. H2009 and H2030 cell lines were used as negative and positive control for YAP1 staining, respectively. Detected somatic *FSTL5* variants are indicated. YAP1 fluorescence micrographs and representative YAP1 immunohistochemistry stains are shown in the right panel. (E) Map of somatic alterations in *FSTL5* detected in all cancers (TCGA), lung adenocarcinoma (TCGA), lung squamous (TCGA), NSCLC cell lines (this study), and human lung tumor samples, 1805 and 1930 (this study). (F) Intersection of the *FSTL5*-dependent and LATS-dependent gene expression programs in *KRAS* mutant/XPO1i sensitive NSCLC lines. To evaluate the enrichment of YAP-responsive genes within the *FSTL5*-dependent gene expression network, quantitative whole-genome transcript (Illumina) arrays were prepared with mRNA isolated from the indicated cell lines treated with the indicated siRNAs 72 hours post-transfection. *LATS1/2* depletion was used to activate YAP-dependent gene expression. All arrays were normalized to corresponding control siRNA treated

samples. Euler plots indicate genes up- or down-regulated at least two fold in response to *siFLST5*, *siLATS* or both and hypergeometric  $p$  values are indicated.

Figure 3. 13

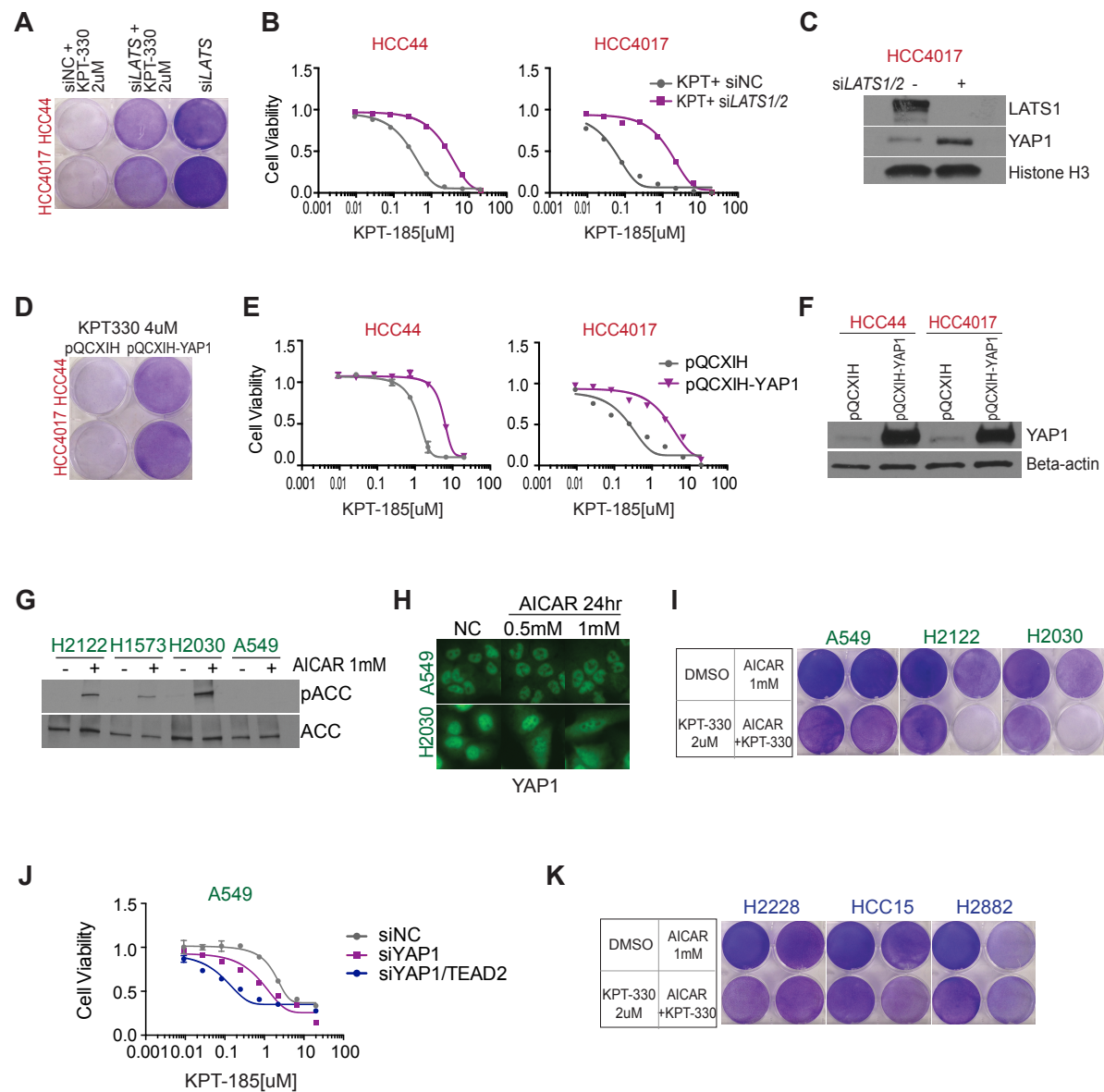


**Figure 3.13. Intrinsic resistance of *KRAS* mutant lines to XPO1 inhibitor is associated with YAP1 activation.**

(A,B) Induction of XPO1i-resistance by *LATS* depletion-mediated YAP pathway activation. 72hr post-transfection with the indicated siRNAs, cells were exposed to XPO1i for 72hrs. Mean of duplicates +/- s.d. is shown in (A). Crystal violet stained monolayers are shown in (B). (C) Immunoblot of the indicated proteins 72hr post-transfection with *LATS1/2* siRNAs. YAP1 accumulation in response to *LATS* depletion is shown. Histone H3 was used as a loading control. (D,E) Induction of XPO1i-resistance by YAP1 overexpression. Proliferating or confluent cells stably expressing indicated plasmids were exposed to XPO1i for 3days and 6 days, respectively. Mean of duplicates +/- s.d. is shown in (D). Crystal violet stained monolayers are shown in (E). (F) Stably overexpressed YAP1 in *KRAS* mutant/XPO1i sensitive lines. Cells were infected with the indicated retroviral vector, selected with hygromycin and then harvested for immunoblotting. (G) Immunoblot of the indicated proteins in *KRAS* mutant/XPO1i resistant lines following a 24hr-exposure to 1mM AICAR. AICAR resulted in accumulation of phospho-Acetyl-CoA-Carboxlyase (pACC), an indicator of AMPK activation in all the lines tested except A549. A549 is known to be non responsive to AICAR due to the absence of LKB1 expression(Kim et al., 2013). (H) Subcellular localization of YAP1 in response to 1mM AICAR. Cells were exposed to 1mM AICAR for 24hrs. Cytoplasmic accumulation of YAP1 was observed in response to AICAR exposure H2030, but not in A549. (I) Induction of XPO1i-sensitivity by AICAR-mediated YAP pathway inhibition. Confluent cultures were exposed to the indicated compounds for 3 days.

(J) Induction of XPO1i-sensitivity by *YAPI/TEAD2* depletion. 48hr post-transfection with the indicated siRNAs, proliferating cultures were exposed to XPO1i for an additional 72 hours. Mean of duplicates +/- s.d. is indicated. (K) Resistance of *KRAS* WT lines to KPT-330 in combination with AICAR. Post-confluent cells were treated as in (I).

**Figure 3. 14**

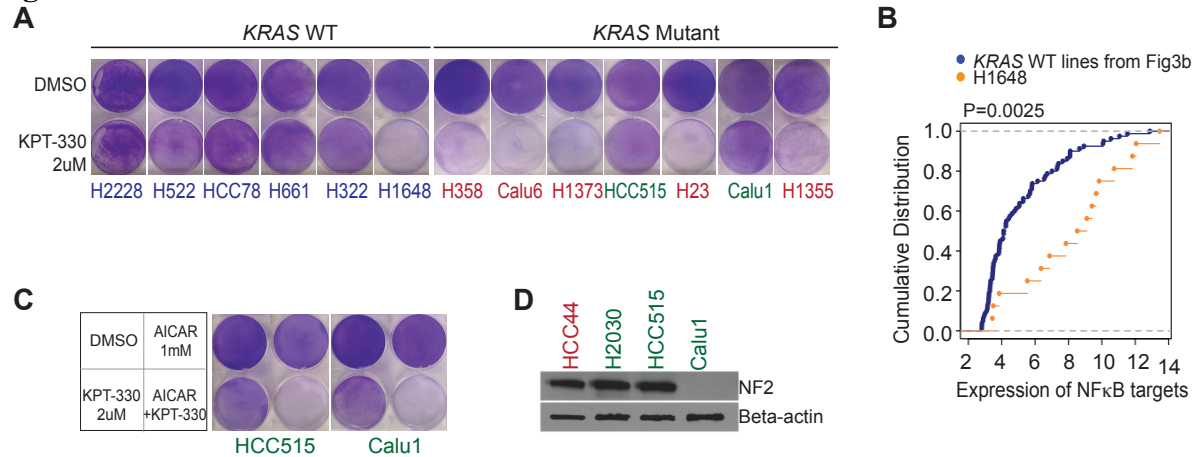


**Figure 3.14. Exceptional responders are accounted for within the mechanistic context of the study as a whole.**

(A) Cytotoxic effect of 2uM KPT-330 on the indicated cell lines. Post-confluent cells were exposed to KPT-330 for 5days. Red labels: *KRAS* mutant/XPO1i-sensitive, Green labels: *KRAS* mutant/XPO1i-resistant, Blue labels: *KRAS* WT. (B) Evidence for NFκB pathway activation in H1648 cells. Empirical cumulative distributions of NFκB target gene expression (from Figure 3.7C) are shown for H1648 versus *KRAS* WT cell lines as indicated. Blue: *KRAS* WT/XPO1i-resistant lines (H2882, HCC15, H1395, H1993, H1819 and HCC95 shown in Figure 3.3 and 3.7), Yellow: *KRAS* WT/XPO1i-sensitive line H1648 . Of note, CCLE data indicates H1648 harbors genomic amplification of *IKKβ*. Blue vs. Yellow,  $P < 0.01$ , KS test. (C) Cytotoxic effect of the indicated compounds on the indicated cell lines. Post-confluent cells were treated as in Figure 3.13I,K. HCC515 harbors a somatic mutation in *LATS1*. (D) Immunoblot of Merlin. Merlin expression is impaired in Calu1 cells.

## DISCUSSION

Collectively, our observations indicate that addiction to XPO1-dependent nuclear/cytoplasmic trafficking is a targetable liability in *KRAS* mutant lung cancer. Therefore clinically available XPO1 inhibitors offer a testable strategy for therapeutic intervention within a currently intractable disease cohort.

Several large-scale loss-of-function studies using RNAi system have attempted to identify synthetic-lethal candidates in the context of oncogenic *KRAS* using panels of cancer cell lines. A difficulty associated with the studies is the huge genetic and phenotypic diversity of cancer cell lines, which may prevent generalization of the synthetic-lethal phenotypes. To address this, we clustered 106 NSCLC based on whole-genome transcript profiles and selected 6 *KRAS* mutant and 6 *KRAS* WT lines that can represent the phenotypic diversity. Another shortcoming of the RNAi screening is high false-positives driven by oligonucleotide sequence specific, but target gene independent, off-target effect (Chapter2). To mitigate this problem, we adopted GSEA and interrogated mechanistic gene sets, rather than individual genes. As a result, we identified a collectively essential biological process, XPO1-dependent nuclear transport, for *KRAS* mutant cells.

XPO1 is a key nuclear export receptor that facilitates cytoplasmic localization of NES containing nuclear proteins. Though it is expected to be significant chemical pleiotropy associated with perturbation of nucleocytoplasmic trafficking of the many XPO1 cargo

proteins, KPT-330 is well tolerated in humans at efficacious doses. To date >1000 patients have been treated with KPT-330 in Phase 1 and Phase 2 clinical trials.

As an underlying mechanism specifying the therapeutic window for XPO1 inhibitors in cell models of *KRAS* lung cancer, we found that selective addiction to I $\kappa$ B nuclear export is a principle component. Our results suggest that *KRAS* mutant cells require XPO1-dependent active nuclear export of I $\kappa$ B to maintain NF $\kappa$ B-mediated survival signaling. Consistently, several groups previously addressed the role of NF $\kappa$ B signaling in oncogenic *KRAS* driven tumor maintenance. Tyler Jacks group has shown that NF $\kappa$ B inhibition via shRNA or expression of dominant-negative form of I $\kappa$ B $\alpha$  resulted in cell death in *Kras*<sup>G12D</sup>/*p53*<sup>-/-</sup> mouse cell lines (Meylan et al., 2009). Albert Baldwin group has demonstrated that *RelA(p65)* null mice displayed significantly lower lung tumor burden in response to oncogenic *KRAS* induction as compared to *RelA(p65)* WT mice. (Basseres et al., 2010)

Of note, we discovered an intrinsic resistance mechanism that involves previously unappreciated loss-of-function mutations in *FSTL5*. Our results showed that *FSTL5* perturbation leads to YAP1 activation and YAP1 activation is sufficient to confer XPO1 inhibitor resistance to otherwise sensitive *KRAS* mutant cells. This finding raises interesting questions to be elucidated. Firstly, how does FSTL5 functionally interact with YAP1? Recent studies show that *Fstl5* depletion promotes tumorigenesis in cooperation with Myc (Zender et al., 2008) and the tumor suppressor function of FSTL5 is possibly associated with its ability to inhibit WNT/  $\beta$ -catenin signaling in hepatocellular carcinoma (Zhang et al., 2015). Given

the previously established interconnection between WNT/ $\beta$ -catenin and YAP1 signaling (Wang et al., 2014; Yu et al., 2015b), it is possible that WNT/ $\beta$ -catenin may participate in functionally linking FSTL5 to YAP1. Another mechanistic scenario is the involvement of inflammasome in FSTL5-mediated YAP1 regulation. FSTL5 was found to physically bind to PYCARD (a.k.a ASC), an adaptor protein of inflammasome (Dowling et al., 2014). And I found that *PYCARD* depletion photocopied *FSTL5* depletion, resulting in YAP1 accumulation (Data not shown). PYCARD can also interact with GP130 (Dowling et al., 2014) and gp130 has been shown to activate Yap1 by engaging tyrosine kinases Src and Yes (Taniguchi et al., 2015). These studies suggest the possibility that FSLT5 may possibly modulate YAP1 through the PYCARD/GP130/SFK signaling axis.

Another important question is how YAP1 regulates the response to XPO1 inhibitors. YAP1 is a transcription coactivator that exerts its function by binding to several transcription factors. In our study, we found that YAP1 cooperates with TEAD2 transcription factor to promote resistance to XPO1 inhibitors (Figure 3.13J). It is, however, not clear which downstream targets of YAP1 are responsible for this process. Further study would provide additional insight into the role of YAP1 in this resistance mechanism.

YAP1 activity can be increased due to the loss of function mutations in *FSTL5* as reported here and mutations in Hippo signaling pathway (Zhao et al., 2010a). These mutations occur in 17% of *KRAS* mutant tumors (TCGA, lung adenocarcinoma). Thus, genomics-guided patient

selection and patient monitoring is anticipated to be an important component to achieve maximum benefit from XPO1 targeted therapy in *KRAS* mutant NSCLCs.

## **MATERIAL AND METHODS**

### **Cell lines and Reagents**

NSCLC cell lines were established at the NCI and The University of Texas Southwestern Medical Center (UTSW; Dallas, TX) or were obtained from the ATCC. They were maintained in RPMI-1640 (Gibco, +L-glutamine/25mM HEPES), supplemented with 5% heat-inactivated fetal bovine serum (FBS, Atlanta Biologicals) and 1% penicillin/streptomycin (Gibco) in a humidified chamber at 5% CO<sub>2</sub>. HBEC30 and HBEC30-KP were maintained in ACL4 (RPMI 1640 [GIBCO, + L-glutamine] supplemented with 0.02 mg/ml insulin, 0.01 mg/ml transferrin, 25 nM sodium selenite, 50 nM hydrocortisone, 10 mM HEPES, 1 ng/ml EGF, 0.01 mM ethanolamine, 0.01 mM O-phosphorylethanolamine, 0.1 nM triiodothyronine, 2 mg/ml BSA, 0.5 mM sodium pyruvate) with 2% FBS and 1% penicillin/streptomycin. All cell lines were authenticated using short tandem repeat (STR) profiling (PowerPlex 1.2; Promega) for at least eight different loci, and results were compared with reference STR profiles available through the ATCC or established by our laboratory. Following authentication, cell line stocks were frozen and maintained in liquid nitrogen until they were used in the reported experiments. Polyclonal stable cell lines (Figure 3.11D, 3.13D-F) were established by infecting parental cells with the

indicated retroviral vector followed by antibiotic selection for 7-14 days. *XPO1*<sup>C528S</sup> knock-in cell lines were generated by CRISPR/Cas9-induced homologous recombination as previously described (Neggers et al., 2015). All cell lines were *Mycoplasma*-tested before experiments (iNtRON biotechnology).

KPT-185 and KPT-330 were provided by Karyopharm Therapeutics. BMS-345541 and Verteporfin were purchased from Sigma. Antibodies were purchased from Cell signaling (cParp #9541, I $\kappa$ B $\alpha$  #4814, YAP1 #12395, LATS1 #3477, Histone H3 #9715, ACC #3676, pACC #3661), Sigma (Beta-actin #A1978), Abcam (Merlin #ab88957) and Santa Cruz Biotechnology (XPO1 #sc5595 and YAP1 #sc101199 for immunofluorescence assay). The mutations (M45A, L49A, I52A) in the nuclear export signal (NES) of *I $\kappa$ B $\alpha$*  were generated using Q5 Site-Directed Mutagenesis Kit (New England Biolabs) and cloned into pEGFP-C3. All siRNAs used for small-scale experiments were from Dharmacon. *LONRF1* siRNA was used as a negative control siRNA.

#### siRNA Screens and Data Processing

Two commercial genome wide siRNA libraries from Ambion (library 1, 21,585 genes) and Dharmacon (library 2, 18,175 genes) were purchased in the 96-well plate format. siRNAs were dissolved in 1X siRNA buffer (Dharmacon) overnight to a final concentration of 10  $\mu$ M and stored at - 80°C prior to use. Library 1 and 2 are mix of 3 and 4 individual siRNA oligos/gene, respectively. Transfection protocols were optimized for each cell line as

previously described (Kim et al., 2013). For reverse transfection 3ul of each siRNA pool (10uM) was transferred to serum-free RPMI (95 ul/well) in empty 96-well assay plates (Costar). 30 ul of this siRNA solution was transferred to an empty 96-well optical assay plate (BioMek), incubated for 5 min, then mixed with 10 ul transfection reagent solution (0.13 ul RNAi Max [Invitrogen] in 10 ul serum free RPMI), and incubated for 15 min. Cells were harvested and diluted in parallel, then added to the siRNA-lipid mix and incubated for 96 hr. All screens were performed using biological triplicates. CellTiter-Glo (Promega) assays were performed using 15 ul reagent/well followed by a 10 min incubation prior to quantitation of luminescence with an Envision plate reader (PerkinElmer). *siUBB* (Dharmacon) was used as a positive control for toxicity for all cell lines. Screen data was row and column median normalized and log2 transformed. Mean values from triplicates were used to calculate batch-centered Z scores using siMacro (Singh et al., 2013).

Hierarchical clustering by UPGMA (unweighted pair group method with arithmetic mean) was performed using the 'stats' package in R based on Euclidean distance using the 'complete' agglomeration method.

### Functional GSEA Analysis

Within each individual cell line, minimum gene-level z-scores were binned according to the following rules:

$$z \leq -3 \rightarrow 3, -3 < z \leq -2 \rightarrow 2, -2 < z \leq -1 \rightarrow 1, z > -1 \rightarrow 0$$

GSEA was then performed with the signal to noise ranking metric to determine gene sets that contained significantly lower z-scores in the *KRAS* mutant cells compared to the *KRAS* wild-type cells. A plot of the running sum and the resulting S2N at each point in the ranked list was constructed in R. The top gene sets preferentially “lower” (containing genes corresponding to siRNA pools with low (toxic) Z-scores) in the *KRAS* mutant cell lines were defined to be those that had a  $P = 0$  and a  $FDR < 0.2$  (Figure 3.2A). We performed a leading edge analysis using the Broad GSEA software to identify genes enriched across multiple significant gene sets (Figure 3.2B).

#### Gene Expression and Data Processing

Raw Illumina HumanWG-6 v3.0 expression beadchip expression files for the NSCLC cell lines used in this study are available from Gene Expression Omnibus using accession number GSE32036. Data were background corrected using the ‘MBCB’ package in R, which provides a model based background correction method similar to an RMA correction with affymetrix arrays. Data were then quantile normalized to produce equivalent expression distributions amongst cell lines.

To evaluate the distribution of expression variation within the NSCLC panel, standard deviations were calculated for expression of each of 25,235 genes (Illumina HumanWG-6 v3.0) across the full panel of 106 NSCLC lines, the 37 *KRAS* mutant NSCLC lines, and the

69 *KRAS* wild-type NSCLC lines. Kernel density estimates were determined using the ‘stats’ package in R.

To examine the gene regulatory pathways affected by XPO1 inhibition, cells were exposed to either DMSO or 1 $\mu$ M KPT-185 for 12hrs. Total mRNA was isolated and gene expression profiling was performed using Illumina HT12v4 chip. Expression values were extracted using GenomeStudio 2010.2. The raw values were background corrected, quantile normalized, log2 transformed and subjected to GSEA.

To examine the transcriptional response to LATS and FSTL5 depletion, cells were first transfected with si*LATS1/2* and si*FSTL5*. 72hrs post-transfection, cells were processed for gene expression profiling as described above. The raw intensities were background corrected, quantile normalized and log2 transformed. Genes with log 2 expression values  $\leq$  4 across the samples (absent) were excluded from further analysis.

For targeted gene expression analysis, total cellular RNA was isolated using RNeasy miniprep Kit (Qiagen). cDNA was then synthesized using High capacity RNA to cDNA kits (Applied biosystems) and subjected to quantitative real-time PCR with TaqMan gene expression assay kits (Applied biosystems).

Unpaired t-test and two sample KS tests were performed using the R ‘stats’ package.

#### Affinity Propagation-based Similarity Clustering Analysis

Clustering analysis was performed with the affinity propagation clustering (APC) algorithm using the ‘apcluster’ package in R. APC is a deterministic clustering method which identifies the number of clusters, and cluster ‘exemplars’ (i.e. the cluster centroid or the data point that is the best representative of all the other data points within that cluster) entirely from the data (Frey and Dueck, 2007), giving it an advantage over non-deterministic methods subject to a biased randomized initialization step, such as Hierarchical Clustering, or methods in which the number of clusters has to be pre-specified, such as k-means clustering.

APC performs clustering by passing messages between the data points. It takes as input a square matrix representing pairwise similarity measures between all data points. The algorithm views each data point as a node in a network and is initialized by connecting all the nodes together where edges between nodes are proportional to Pearson correlations. The algorithm then iteratively transmits messages along the edges, pruning edges with each iteration, until a set of clusters and exemplars emerges.

Two real valued messages are passed between nodes. The ‘responsibility’ message computes how well suited it is for point  $i$  to choose point  $k$  as an exemplar, given all the other candidate exemplars,  $k'$ , and is updated by:

$$r(i, k) \leftarrow s(i, k) - \max_{k' \neq k} \{a(i, k') + s(i, k')\}$$

The availability message,  $a(i, k)$ , computes how appropriate it is for point  $i$  to select point  $k$  as an exemplar, taking into account all the other points for which  $k$  is an exemplar,  $i'$ , and is given by:

$$a(i, k) \leftarrow \min \left\{ 0, r(k, k) + \sum_{i' \text{ st } i' \notin \{i, k\}} \max(0, r(i', k)) \right\}$$

In the above equation,  $a(i, k)$  is set to the self responsibility,  $r(k, k)$ , plus the sum of the positive responsibilities candidate  $k$  receives from other points. The entire sum is thresholded at 0, and a negative availability indicates that it is inappropriate for point  $i$  to chose point  $k$  as an exemplar and the tie is severed. The self-availability,  $a(k, k)$ , reflects the accumulated evidence that point  $k$  is an exemplar and is updated with the following rule, which reflects the evidence that  $k$  is an exemplar based on the positive responsibilities sent to  $k$  from all points, and is updated by:

$$a(k, k) \leftarrow \sum_{i' \text{ st } i' \notin \{i, k\}} \max(0, r(i', k))$$

In the first iteration, all points are considered equally likely to be candidate exemplars, and  $a(i, k)$  is set to 0 and  $s(i, k)$  is set to the input similarity measure between points  $i$  and  $k$ . The above rules are then iteratively updated until a clear, stable set of clusters and exemplars emerges.

In our implementation, we first used the algorithm to identify an initial set of exemplars and clusters from the data matrix. The exemplars were then clustered together and this procedure was repeated until no more clusters emerged to identify a hierarchical structure of clusters. Networks were drawn with cytoscape (Shannon et al., 2003) in the following manner. All members of the primary clusters are interconnected, and edge lengths are drawn to be proportional to Euclidean distances. Edge lengths between exemplars that cluster together are

also drawn to be proportional to Euclidean distances. The entire map was rendered in a 2 dimensional display using a cytoscape built-in spring embedded algorithm.

To cluster 106 NSCLC cell lines with defined *KRAS* status by similar expression profiles (Figure 3.1A), we first reduced the panel of genes to those that were expressed at a log2 normalized expression value of 6 in at least one cell line and those that were present in the top 20% of the most highly variant genes; resulting in a panel of 3101 detectable and variable genes.

#### Retrospective Analysis of Genome-wide Synthetic-lethal shRNA Screen Data

Figure 3.2E was generated from genome-wide synthetic-lethal shRNA screening data(Luo et al., 2009). The shRNA screen was performed in an isogenic pair of *KRAS* wild-type and *KRAS*<sup>G12D</sup> colorectal cancer cell lines with 6 pools of ~13000 shRNAs/pool targeting 32,293 human transcripts. Log2 fold-changes in relative abundance of each shRNAs depleted over time were analyzed for each sample. Those with a fold-depletion equal or less than 0 in any sample were then compared between samples (*KRAS* mutant versus *KRAS* wild-type) using the non-parametric two-sample KS test.

#### Cell Viability and Cytotoxicity Assay

For dose-response curves, cells were plated at 50% density in 96-well assay plates. On the following day, serially diluted compounds or carrier alone were added to the culture media.

Cell viability was measured using CellTiter-Glo (Promega) 72hr post-treatment. For dose-response analysis of XPO1 inhibitors combined with either siRNAs or chemical inhibitors (Figure 3.8A, 3.11A,B 3.13B,E,J), cell viability was normalized to indicated matching controls. Area Under the dose-response Curves (AUCs) was computed by the trapezoidal method using GradPad software. Caspase enzymatic activity was analyzed using Caspase-Glo 3/7 (Promega) after compound treatment according to manufacture's instructions. The raw luminescence values were divided with the average luminescence values of matching controls (Figure 3.3F, 3.8C). To examine the cytotoxic effect of compounds on post-confluent cells, NSCLC cells were cultured to confluence in 6-well plates, exposed to compounds as indicated, then fixed with 100% cold methanol for 10 min. and stained with 0.5% crystal violet for 30 min. at room temperature. To examine tolerance to ectopic expression of nuclear I $\kappa$ B $\alpha$ , test plasmid DNAs (pEGFP-C3-I $\kappa$ B $\alpha$ -NES-Mut) and control plasmid DNAs (pEGFP-C3) were delivered to H2882 cells and H2009 cells in 12-well plates. 48 and 72hrs after transfection, cells were fixed and GFP/DAPI ratio was examined using images taken with a Zeiss Plan 20 $\times$ /0,30 PH1 objective on a Zeiss Axioplan 2E microscope. The following formula was used:

$$\text{Sensitivity to Nuclear I}\kappa\text{B}\alpha \text{ (Viability)} = \frac{\text{GFP-I}\kappa\text{B}\alpha\text{-NES-Mut}}{\text{DAPI}} \div \frac{\text{GFP-empty}}{\text{DAPI}}$$

Proliferation Rate Measurement of NSCLC lines

Cells were counted at seeding, allowed to grow to a confluence of 80-90% and then harvested and total cell number was determined. Population doubling time was calculated using the following formula: Number of hours from seeding to harvest/[ $((\log N(t) - \log N(t_0))/\log 2)$ ].  $N(t)$  is the number of cells at time of passage and  $N(t_0)$  is the number of cells seeded at previous passage (Bruckova et al., 2011).

#### Targeted siRNA and Plasmid DNA Transfection

For transfection in 96-well plates, 1  $\mu$ l siRNA (10  $\mu$ M) in 30  $\mu$ l of serum-free RPMI was mixed with 0.4  $\mu$ l of RNAi Max (Invitrogen) in 10  $\mu$ l of serum-free RPMI. Following a 15 min incubation, the siRNA-lipid mix was transferred to empty 96-well assay plates followed by delivery of single cell suspensions (100  $\mu$ l/well). For transfection in 6-well plates, 10  $\mu$ l siRNA (10  $\mu$ M) in 250  $\mu$ l of serum-free RPMI was mixed with 7  $\mu$ l RNAi Max in 250  $\mu$ l of serum-free RPMI and were delivered to plates followed by delivery of single-cell suspensions (2 ml/well). For plasmid DNA transfection in 12-well plates, 0.5  $\mu$ g of plasmid DNA in 25  $\mu$ l of serum-free media was mixed with 1.5  $\mu$ l Fugene 6 (Promega) in 25  $\mu$ l of serum-free media. After a 15 min incubation, suspended cells (1 ml/well) were added to the plate with DNA-Fugene 6 complexes. In 60 mm dishes, cells were pre-plated and then 2  $\mu$ g DNA/6  $\mu$ l Fugene 6 complexes in 100  $\mu$ l of serum-free media were delivered to the cells the next day.

### NFkB Transcriptional Activity Reporter Assay

Cells were reverse-transfected in 96-well microtiter plate format with a reporter plasmid (pGL4.32[luc2p/NFkB-RE/Hygro], Promega) expressing firefly luciferase under the control of multimerized NFkB responsive element together with the pRL-SV40 Renilla luciferase control reporter plasmid at a ratio of 9:1. 24hrs post-transfection, cells were exposed to compounds as indicated for 24hrs and then treated with 4ng/ml TNF $\alpha$  for 6hrs. Luciferase activities were measured using the Dual luciferase reporter system (Promega) according to manufacture's instructions.

### Mouse Xenografts

NOD/SCID female mice at 4-9 weeks of age were injected subcutaneously with H2882 ( $3 \times 10^5$ ) cells, H2009 ( $5 \times 10^5$ ) cells, and H460 ( $2.5 \times 10^5$ ) cells. When tumors reached 100mm<sup>3</sup> or larger, mice were randomly assigned to three cohorts and orally treated with carrier (0.6% w/v PVP K-29/32 and 0.6% w/v Pluronic F-68), 3mg/kg, or 10mg/kg KPT-330 three times a week by oral gavage. Tumor volume was monitored with digital caliper using the following formula:  $\text{Width}^2 \times \text{Length} / 2$ . Nutri-Cal (Tomlyn) was provided to mice throughout the experiment as a nutritional supplement. The number of mice per cohort was as follows: for H2882 xenografts, carrier, n=7; 3mg/kg, n=7; 10mg/kg, n=6; for H2009 xenografts, carrier, n=9; 3mg/kg, n=8; 10mg/kg, n=9; for H460 xenografts, carrier, n=4, 3mg/kg, n=5, 10mg/kg, n=5.

For bioanalysis of KPT-330 in mouse plasma, plasma samples were collected by cardiac puncture from mice (n=4/group), processed with three volumes of methanol containing internal standard (propranolol) and then centrifuged at 1000 g for 10min. The supernatant was analyzed by LC/MS/MS using an Agilent 6410 mass spectrometer coupled with an Agilent 1200 HPLC and a CTC PAL chilled autosampler, all controlled by MassHunter software (Agilent). After separation on a C18 reverse phase HPLC column (Agilent) using an acetonitrile-water gradient system, peaks were analyzed by mass spectrometry using ESI ionization in MRM mode. All plasma samples were compared to a calibration curve prepared in mouse blank plasma.

*K-ras*<sup>LSL-G12D</sup> / *p53*<sup>fl/fl</sup> GEM model

*K-ras*<sup>LSL-G12D</sup> / *p53*<sup>fl/fl</sup> mice were infected with 2.5X10<sup>7</sup> PFU of Ad-Cre (University of Iowa, Gene Transfer Vector Core) intratracheally at 7-8 weeks of age as previously described (DuPage et al., 2009). Eight to ten weeks after the injection, tumor development was monitored by MR imaging before treatment. Mice with equivalent tumor burden were randomly assigned to two cohorts and orally treated with either carrier (0.6% w/v PVP K-29/32 and 0.6% w/v Pluronic F-68; n=3) or 10mg/kg KPT-330 (n=4) three times a week by oral gavage. Outlier animals presenting with exceptionally high tumor burden were treated with 10mg/kg KPT-330 five times a week by oral gavage. After the three weeks of treatment, lungs were imaged with MRI, then harvested, fixed with 10% formalin, paraffin-embedded,

and H&E stained. The stained lung tissue specimens were scanned in Hamamatsu Nanozoomer 2.0HT for visualization and evaluation. Tumor burden was determined on the largest lobe and calculated as the tumor area divided by lung area. Area of interest was quantified using Image J software.

All MR images were obtained using a 7T small animal MRI scanner (Agilent (Varian), Inc, Palo Alto, CA) equipped with a 40 mm Millipede RF coil (ExtendMR LLC, Milpitas, CA). All MRI acquisitions were gated using both cardiac and respiratory triggering. The images were recorded on the transverse plane, with the major parameters as follows: The repetition time (TR) = 200, the echo time (TE) = 1.834 ms, the flip angle (FA) = 45°, the number of average = 8, the field of view (FOV) = 32 x 32 mm<sup>2</sup>, the matrix size = 256 x 256, the slice number = 17, and the slice thickness = 1 mm without any gap.

#### Patient-derived Xenografts

Human *KRAS*<sup>G12D</sup> T2aN0Mx stage lung adenocarcinoma tissue was obtained from a 40-year-old lung cancer patient and directly implanted into the liver capsule of a NOD/SCID mouse. The mouse was sacrificed eighteen weeks later and the engrafted tumor was harvested, divided, frozen in 10% DMSO /90% FBS and stored at -80C until being re-implanted subcutaneously to another NOD/SCID mouse in both flanks. When the tumors reached to ~10mm in length, the tumors were resected, evenly divided into 19 pieces and re-implanted subcutaneously to 10 week-old NOD/SCID female mice. Mice harboring palpable engrafted

tumors (58~101mm<sup>3</sup>) were randomly assigned to receive either carrier (0.6% w/v PVP K-29/32 and 0.6% w/v Pluronic F-68; n=6) or 10mg/kg KPT-330 (n=6) three times a week. Tumor volume was monitored with digital caliper using the following formula:  $\text{Width}^2 \times \text{Length} / 2$ .

All mouse studies were performed according to the guidelines of the UT southwestern Institutional Animal Care and Use Committee.

#### Immunofluorescence and Immunohistochemistry

For immunofluorescence-based imaging, cells were fixed with 3.7% formaldehyde (Fisher Scientific), permeabilized with 0.1% Triton X-100, blocked with PBST (PBS containing 1% bovine serum albumin and 0.1% Tween-20) and incubated with antibodies in PBST against the indicated proteins. Representative images were captured with a PCO: sCMOS 5.5 CAMERA on a Zeiss Axioplan 2E microscope.

For immunohistochemistry (IHC)-based protein expression analysis, paraffin-embedded mouse tumor samples were deparaffinized, subjected to heat-induced antigen-retrieval in 10 mM sodium citrate buffer, blocked using 3% peroxidase (Sigma), Avidin/Biotin blocking Kit(Vector laboratories), and M.O.M. Kit (Vector laboratories) and incubated with anti-IkBa antibody (Cell signaling, 1:50) and then biotinylated secondary antibody followed by ABC reagent (Vector laboratories). The samples were stained using immPACT DAB (Vector laboratories) and counter stained using Mayer's hematoxylin solution (Sigma).

In tissue microarray with patient-derived lung tumor samples, IHC reaction was performed using a Leica Bond Max automated stainer (Leica Biosystems, Nussloch GmbH). In summary, the NSCLC TMA slides were deparaffinized and hydrated in the Leica Bond autostainer. The primary antibodies employed were YAP1 (rabbit monoclonal, clone D8H1X, Cell Signaling Technology, cat#14074, 1:100). Antigen retrieval was done with Bond Epitope Retrieval Solution No. 1 (Ref # AR9961, Leica Biosystems, equivalent to citrate buffer pH 6.0). The IHC reaction was detected using the Bond Polymer Refine Detection (Ref # DS98000, Leica Biosystems) with diaminobenzidine as chromogen for the visualization of the staining. The slides were counterstained with hematoxylin (Leica Biosystems). Formalin fixed paraffin embedded (FFPE) human breast and colon adenocarcinomas were employed as positive controls. Non-primary antibody control was also used as an additional control. All TMA slides were stained for YAP1 at the same time with the controls and cell line samples. The stained slides were scanned in an Aperio AT Turbo digital pathology system (Leica Biosystems) for visualization and evaluation. IHC quality control and scoring were performed by two pathologists (Pamela Villalobos and Jaime Rodriguez-Canales). The IHC scoring system employed was H-score, which evaluate intensity (0 to 3) and percentage of positive tumor cells (0 to 100), with a final scoring ranging from 0 to 300.

The tissue microarrays used in this study comprised 37 surgically resected lung adenocarcinoma tumors. All specimens were collected from the lung cancer tissue bank at

The University of Texas M. D. Anderson Cancer Center, which is approved by the M.D. Anderson institutional review board. After histologic examination, tissue microarrays were constructed using three 1-mm-diameter cores per tumor. Tissue microarrays were prepared with a semi-automatic tissue arrayer (Veridiam Tissue Arrayer Model VTA-100, Veridiam, Oceanside, CA) using 1 mm diameter cores in triplicate for tumors, as described previously (Sun et al., 2009). Histologic sections that were 4  $\mu$ m in thickness were then prepared for the subsequent immunohistochemical analysis. Clinical and pathologic information was obtained for all patients (Supplementary Table 12). Pathologic tumor-node-metastasis stage had been determined for lung cancers at time of primary tumor surgery.

#### Whole-exome Deep Sequencing and Targeted Sanger Sequencing

Genomic DNA from NSCLC lines and patient-matched B-cell lines was isolated using DNeasy Blood and Tissue Kits (QIAGEN). Exonic DNA was captured using SureSelect 38MB All Exon Kit (Agilent) following manufacturer's protocol, and sequenced using HySeq 2000 (Illumina) with a paired-end sequencing protocol and reads were aligned to NCBI human genome as previously described by Bowtie 0.12.5 (Kim et al., 2013; Langmead et al., 2009) allowing up to 2 mismatches per read. Single-nucleotide variants (SNV) were discovered from the uniquely aligned reads with at least one mismatch with a phred quality score greater than 20 and coverage greater than 6 by nonredundant reads. Somatic SNVs were identified by requiring coverage on the variant site by wild-type allele to be greater than

6 and by mutant allele to be 0. A series of filters was used to filter out probable germline mutations from somatic mutations identified in NSCLC cell lines without a matched normal B-cell line. They are as follows:

1) Germline variants that were found in the matched dataset were removed. 2) Variants that were found to be present in dbSNP but not in COSMIC were removed. 3) Silent, intergenic, and UTR variants were removed. 4) Variants that were found at a frequency  $\geq 8\%$  in the thousand genome project were removed. 5) Variants in genes that were mutated  $\geq 62$  times at any site across the panel were removed. 6) Variants that were mutated at the same amino acid position in greater than 9 cell lines were removed, however, we rescued back variants that were found to be ‘hotspots’ in the matched dataset.

For targeted detection of mutations in *FSTL5*, genomic DNA was extracted from patient-derived human lung tumor samples and matched normal tissues. Exons 2 through 16 were amplified by PCR with HotStarTqa Mater Mix kit (Qiagen), purified using USB ExoSAP-IT (Affymetrix) and Sanger sequenced. For exons that exhibited mixed chromatograms, PCR products were cloned using TOPO TA cloning Kit (Invitrogen) and the resulting clones were individually sequenced.

### Bicluster Analysis

We converted the mutation table to a binary presence call table where a ‘1’ indicated presence of mutation in a cell line and ‘0’ indicated wild-type. We created a biclustering

script that searches for every possible permutation of rows (genes) and columns (cell lines) to identify the biggest blocks of 1's in the dataset. In other words, we search for the largest number of mutations that are shared by the largest number of cell lines. We then identified the bicluster that identified mutations that were shared by *KRAS* mutant/XPO1 inhibitor-resistant lines that were not present in the *KRAS* mutant/XPO1 inhibitor-sensitive lines. This bicluster contained the single gene *FSTL5*.

#### Retrospective Analysis of shRNA Enrichment in HCC

Figure 3.11E was generated from an oncogenomics-based in vivo RNAi screening result (Table S3)(Zender et al., 2008). Shown are 36 shRNAs enriched at least 2.5 fold over the predicted representation during HCC tumor development.

#### ACKNOWLEDGEMENTS

This work could not have been achieved without my valuable colleagues and collaborators. I wish to thank Hyunseok Kim, Saurabh Mendiratta, Shuguang Wei and HTS core for whole-genome siRNA screening efforts; Elizabeth McMillan for her tremendous help with gene expression/exome sequencing data processing and analysis; Niranjan Venkateswaran, Drs. Pier Paolo Scaglioni, John Minna, Boning Gao, Shanrong Zhang for their advice and technical help with mouse experiments; Dr. Dirk Daelemans, Jasper Neggers (KU university)

for XPO1 C528S knock-in cell lines; Robin Frink for cell proliferation rate data; Karyopharm for KPT compounds; Dr. Ignacio group (MD Anderson) for YAP1 tissue microarray; Gurbani Makkar for her technical help.

## CHAPTER FOUR

### CONCLUDING REMARKS

*KRAS* is a major driver oncogene frequently activated by single point mutations in ~30% of NSCLCs. The oncogenic *KRAS* mutations can be easily detected in patient samples; however, its clinical utility is very limited due to lack of effective targeted therapies. Here we showed that *KRAS* mutant NSCLC cells are selectively addicted to XPO1-dependent nuclear export and therefore, XPO1 can represent a promising potential strategy for *KRAS* mutant NSCLC. Based on this finding, we are currently planning to develop and launch clinical trials to evaluate the efficacy of Seliexor (KPT-330, XPO1 inhibitor) in combination with conventional chemotherapy over single-agent chemotherapy in *KRAS* mutant lung cancer. Of note, our results revealed that a subset of *KRAS* mutant NSCLC lines bypasses XPO1 addiction via YAP1 activation, which can represent intrinsic and acquired resistance mechanisms. An estimated 17% of all *KRAS* mutant lung tumor cases are expected to have YAP1 activation, suggesting that YAP1 expression in patient samples could potentially serve as a prognostic biomarker.

I hope this work helps lead to new promising therapeutic approaches that may one day allow us to overcome *KRAS* mutant lung cancer.

## BIBLIOGRAPHY

Ahearn, I.M., Haigis, K., Bar-Sagi, D., and Philips, M.R. (2012). Regulating the regulator: post-translational modification of RAS. In *Nat. Rev. Mol. Cell Biol.*, pp. 39-51.

American Cancer Society (2016). *Cancer Facts & Figures 2016*.

Bai, D., Ueno, L., and Vogt, P.K. (2009). Akt-mediated regulation of NFkappaB and the essentialness of NFkappaB for the oncogenicity of PI3K and Akt. *International journal of cancer* 125, 2863-2870.

Barbie, D.A., Tamayo, P., Boehm, J.S., Kim, S.Y., Moody, S.E., Dunn, I.F., Schinzel, A.C., Sandy, P., Meylan, E., Scholl, C., *et al.* (2009). Systematic RNA interference reveals that oncogenic KRAS-driven cancers require TBK1. *Nature* 462, 108-112.

Bartel, D.P. (2009). MicroRNAs: target recognition and regulatory functions. In *Cell*, pp. 215-233.

Basseres, D.S., Ebbs, A., Cogswell, P.C., and Baldwin, A.S. (2014). IKK is a therapeutic target in KRAS-Induced lung cancer with disrupted p53 activity. *Genes & cancer* 5, 41-55.

Basseres, D.S., Ebbs, A., Levantini, E., and Baldwin, A.S. (2010). Requirement of the NF-kappaB subunit p65/RelA for K-Ras-induced lung tumorigenesis. *Cancer research* 70, 3537-3546.

Basu, S., Totty, N.F., Irwin, M.S., Sudol, M., and Downward, J. (2003). Akt phosphorylates the Yes-associated protein, YAP, to induce interaction with 14-3-3 and attenuation of p73-mediated apoptosis. *Molecular cell* 11, 11-23.

Baumann, B., Weber, C.K., Troppmair, J., Whiteside, S., Israel, A., Rapp, U.R., and Wirth, T. (2000). Raf induces NF-kappaB by membrane shuttle kinase MEKK1, a signaling pathway critical for transformation. *Proceedings of the National Academy of Sciences of the United States of America* 97, 4615-4620.

Beg, A.A., and Baldwin, A.S., Jr. (1993). The I kappa B proteins: multifunctional regulators of Rel/NF-kappa B transcription factors. *Genes & development* 7, 2064-2070.

Bodemann, B.O., and White, M.A. (2008). Ral GTPases and cancer: linchpin support of the tumorigenic platform. In *Nat. Rev. Cancer*, pp. 133-140.

Bruckova, L., Soukup, T., Visek, B., Moos, J., Moosova, M., Pavelkova, J., Rezabek, K., Kucerova, L., Micuda, S., Brackova, E., *et al.* (2011). Proliferative potential and phenotypic analysis of long-term cultivated human granulosa cells initiated by addition of follicular fluid. *Journal of assisted reproduction and genetics* 28, 939-950.

Burke, J.R., Pattoli, M.A., Gregor, K.R., Brassil, P.J., MacMaster, J.F., McIntyre, K.W., Yang, X., Iotzova, V.S., Clarke, W., Strnad, J., *et al.* (2003). BMS-345541 is a highly

selective inhibitor of I kappa B kinase that binds at an allosteric site of the enzyme and blocks NF-kappa B-dependent transcription in mice. *The Journal of biological chemistry* 278, 1450-1456.

Cancer Genome Atlas Research, N. (2012). Comprehensive genomic characterization of squamous cell lung cancers. *Nature* 489, 519-525.

Cancer Genome Atlas Research, N. (2014). Comprehensive molecular profiling of lung adenocarcinoma. *Nature* 511, 543-550.

Castellano, E., and Downward, J. (2011). RAS Interaction with PI3K: More Than Just Another Effector Pathway. In *Genes & cancer*, pp. 261-274.

Chang, F., Steelman, L.S., Lee, J.T., Shelton, J.G., Navolanic, P.M., Blalock, W.L., Franklin, R.A., and McCubrey, J.A. (2003). Signal transduction mediated by the Ras/Raf/MEK/ERK pathway from cytokine receptors to transcription factors: potential targeting for therapeutic intervention. *Leukemia* 17, 1263-1293.

Cheng, Y., Holloway, M.P., Nguyen, K., McCauley, D., Landesman, Y., Kauffman, M.G., Shacham, S., and Altura, R.A. (2014). XPO1 (CRM1) inhibition represses STAT3 activation to drive a survivin-dependent oncogenic switch in triple-negative breast cancer. *Molecular cancer therapeutics* 13, 675-686.

Chien, Y., and White, M.A. (2003). RAL GTPases are linchpin modulators of human tumour-cell proliferation and survival. In *EMBO reports*, pp. 800-806.

Corcoran, R.B., Cheng, K.A., Hata, A.N., Faber, A.C., Ebi, H., Coffee, E.M., Greninger, P., Brown, R.D., Godfrey, J.T., Cohoon, T.J., *et al.* (2013). Synthetic lethal interaction of combined BCL-XL and MEK inhibition promotes tumor regressions in KRAS mutant cancer models. *Cancer cell* 23, 121-128.

Doench, J.G., Petersen, C.P., and Sharp, P.A. (2003). siRNAs can function as miRNAs. *Genes & development* 17, 438-442.

Dowling, J.K., Becker, C.E., Bourke, N.M., Corr, S.C., Connolly, D.J., Quinn, S.R., Pandolfi, P.P., Mansell, A., and O'Neill, L.A. (2014). Promyelocytic leukemia protein interacts with the apoptosis-associated speck-like protein to limit inflammasome activation. *The Journal of biological chemistry* 289, 6429-6437.

DuPage, M., Dooley, A.L., and Jacks, T. (2009). Conditional mouse lung cancer models using adenoviral or lentiviral delivery of Cre recombinase. *Nature protocols* 4, 1064-1072.

Dupont, S., Morsut, L., Aragona, M., Enzo, E., Giulitti, S., Cordenonsi, M., Zanconato, F., Le Digabel, J., Forcato, M., Bicciato, S., *et al.* (2011). Role of YAP/TAZ in mechanotransduction. *Nature* 474, 179-183.

- Elbashir, S.M., Lendeckel, W., and Tuschl, T. (2001). RNA interference is mediated by 21- and 22-nucleotide RNAs. *Genes & development* 15, 188-200.
- Fitamant, J., Kottakis, F., Benhamouche, S., Tian, H.S., Chuvain, N., Parachoniak, C.A., Nagle, J.M., Perera, R.M., Lapouge, M., Deshpande, V., *et al.* (2015). YAP Inhibition Restores Hepatocyte Differentiation in Advanced HCC, Leading to Tumor Regression. *Cell reports*.
- Frey, B.J., and Dueck, D. (2007). Clustering by passing messages between data points. *Science* 315, 972-976.
- Gerondakis, S., Grossmann, M., Nakamura, Y., Pohl, T., and Grumont, R. (1999). Genetic approaches in mice to understand Rel/NF-kappaB and IkappaB function: transgenics and knockouts. In *Oncogene*, pp. 6888-6895.
- Gysin, S., Salt, M., Young, A., and McCormick, F. (2011). Therapeutic strategies for targeting ras proteins. *Genes & cancer* 2, 359-372.
- Hayden, M.S., and Ghosh, S. (2012). NF-κB, the first quarter-century: remarkable progress and outstanding questions. In *Genes Dev. (Cold Spring Harbor Lab)*, pp. 203-234.
- He, L., and Hannon, G.J. (2004). MicroRNAs: small RNAs with a big role in gene regulation. In *Nat. Rev. Genet.*, pp. 522-531.
- Hoesel, B., and Schmid, J.A. (2013). The complexity of NF-κB signaling in inflammation and cancer. In *Mol. Cancer (BioMed Central)*, p. 86.
- Jackson, A.L., Bartz, S.R., Schelter, J., Kobayashi, S.V., Burchard, J., Mao, M., Li, B., Cavet, G., and Linsley, P.S. (2003). Expression profiling reveals off-target gene regulation by RNAi. *Nature biotechnology* 21, 635-637.
- Jackson, A.L., Burchard, J., Schelter, J., Chau, B.N., Cleary, M., Lim, L., and Linsley, P.S. (2006). Widespread siRNA "off-target" transcript silencing mediated by seed region sequence complementarity. *Rna* 12, 1179-1187.
- Jancik, S., Drabek, J., Radzioch, D., and Hajduch, M. (2010). Clinical relevance of KRAS in human cancers. *Journal of biomedicine & biotechnology* 2010, 150960.
- Jancík, S., Drábek, J., Radzioch, D., and Hajdúch, M. (2010). Clinical relevance of KRAS in human cancers. In *J. Biomed. Biotechnol.*, pp. 150960-150913.
- Johnson, R., and Halder, G. (2014). The two faces of Hippo: targeting the Hippo pathway for regenerative medicine and cancer treatment. *Nature reviews. Drug discovery* 13, 63-79.

- Kapoor, A., Yao, W., Ying, H., Hua, S., Liewen, A., Wang, Q., Zhong, Y., Wu, C.J., Sadanandam, A., Hu, B., *et al.* (2014). Yap1 activation enables bypass of oncogenic Kras addiction in pancreatic cancer. *Cell* 158, 185-197.
- Karnoub, A.E., and Weinberg, R.A. (2008). Ras oncogenes: split personalities. In *Nat. Rev. Mol. Cell Biol.* (Nature Publishing Group), pp. 517-531.
- Kim, H.S., Mendiratta, S., Kim, J., Pecot, C.V., Larsen, J.E., Zubovych, I., Seo, B.Y., Kim, J., Eskiciok, B., Chung, H., *et al.* (2013). Systematic identification of molecular subtype-selective vulnerabilities in non-small-cell lung cancer. *Cell* 155, 552-566.
- Kumar, M.S., Hancock, D.C., Molina-Arcas, M., Steckel, M., East, P., Diefenbacher, M., Armenteros-Monterroso, E., Lassailly, F., Matthews, N., Nye, E., *et al.* (2012). The GATA2 transcriptional network is requisite for RAS oncogene-driven non-small cell lung cancer. *Cell* 149, 642-655.
- Langmead, B., Trapnell, C., Pop, M., and Salzberg, S.L. (2009). Ultrafast and memory-efficient alignment of short DNA sequences to the human genome. *Genome biology* 10, R25.
- Levy, D., Adamovich, Y., Reuven, N., and Shaul, Y. (2008). Yap1 phosphorylation by c-Abl is a critical step in selective activation of proapoptotic genes in response to DNA damage. *Molecular cell* 29, 350-361.
- Lim, S.M., Westover, K.D., Ficarro, S.B., Harrison, R.A., Choi, H.G., Pacold, M.E., Carrasco, M., Hunter, J., Kim, N.D., Xie, T., *et al.* (2014). Therapeutic targeting of oncogenic K-Ras by a covalent catalytic site inhibitor. *Angewandte Chemie* 53, 199-204.
- Lin, L., Sabnis, A.J., Chan, E., Olivas, V., Cade, L., Pazarentzos, E., Asthana, S., Neel, D., Yan, J.J., Lu, X., *et al.* (2015a). The Hippo effector YAP promotes resistance to RAF- and MEK-targeted cancer therapies. *Nature genetics* 47, 250-256.
- Lin, X., Ruan, X., Anderson, M.G., McDowell, J.A., Kroeger, P.E., Fesik, S.W., and Shen, Y. (2005). siRNA-mediated off-target gene silencing triggered by a 7 nt complementation. *Nucleic acids research* 33, 4527-4535.
- Lin, Z., Zhou, P., von Gise, A., Gu, F., Ma, Q., Chen, J., Guo, H., van Gorp, P.R., Wang, D.Z., and Pu, W.T. (2015b). Pi3kcb links Hippo-YAP and PI3K-AKT signaling pathways to promote cardiomyocyte proliferation and survival. *Circulation research* 116, 35-45.
- Ling, J., Kang, Y.a.a., Zhao, R., Xia, Q., Lee, D.-F., Chang, Z., Li, J., Peng, B., Fleming, J.B., Wang, H., *et al.* (2012). KrasG12D-induced IKK2/ $\beta$ /NF- $\kappa$ B activation by IL-1 $\alpha$  and p62 feedforward loops is required for development of pancreatic ductal adenocarcinoma. In *Cancer cell*, pp. 105-120.

- Luo, J., Emanuele, M.J., Li, D., Creighton, C.J., Schlabach, M.R., Westbrook, T.F., Wong, K.K., and Elledge, S.J. (2009). A genome-wide RNAi screen identifies multiple synthetic lethal interactions with the Ras oncogene. *Cell* *137*, 835-848.
- Marine, S., Bahl, A., Ferrer, M., and Buehler, E. (2012). Common seed analysis to identify off-target effects in siRNA screens. *Journal of biomolecular screening* *17*, 370-378.
- May, M.J., and Ghosh, S. (1998). Signal transduction through NF-kappa B. In *Immunol. Today*, pp. 80-88.
- Mayo, M.W., Wang, C.Y., Cogswell, P.C., Rogers-Graham, K.S., Lowe, S.W., Der, C.J., and Baldwin, A.S. (1997). Requirement of NF-kappaB activation to suppress p53-independent apoptosis induced by oncogenic Ras. In *Science*, pp. 1812-1815.
- Meylan, E., Dooley, A.L., Feldser, D.M., Shen, L., Turk, E., Ouyang, C., and Jacks, T. (2009). Requirement for NF-kappaB signalling in a mouse model of lung adenocarcinoma. *Nature* *462*, 104-107.
- Mo, J.S., Meng, Z., Kim, Y.C., Park, H.W., Hansen, C.G., Kim, S., Lim, D.S., and Guan, K.L. (2015). Cellular energy stress induces AMPK-mediated regulation of YAP and the Hippo pathway. *Nature cell biology* *17*, 500-510.
- Neggers, J.E., Vercruysse, T., Jacquemyn, M., Vanstreels, E., Baloglu, E., Shacham, S., Crochiere, M., Landesman, Y., and Daelemans, D. (2015). Identifying drug-target selectivity of small-molecule CRM1/XPO1 inhibitors by CRISPR/Cas9 genome editing. *Chemistry & biology* *22*, 107-116.
- Oeckinghaus, A., Hayden, M.S., and Ghosh, S. (2011). Crosstalk in NF-kappaB signaling pathways. *Nature immunology* *12*, 695-708.
- Ostrem, J.M., Peters, U., Sos, M.L., Wells, J.A., and Shokat, K.M. (2013). K-Ras(G12C) inhibitors allosterically control GTP affinity and effector interactions. *Nature* *503*, 548-551.
- Pao, W., and Hutchinson, K.E. (2012). Chipping away at the lung cancer genome. *Nature medicine* *18*, 349-351.
- Phelps, R.M., Johnson, B.E., Ihde, D.C., Gazdar, A.F., Carbone, D.P., McClintock, P.R., Linnoila, R.I., Matthews, M.J., Bunn, P.A., Jr., Carney, D., *et al.* (1996). NCI-Navy Medical Oncology Branch cell line data base. *Journal of cellular biochemistry. Supplement* *24*, 32-91.
- Roberts, P.J., and Stinchcombe, T.E. (2013). KRAS mutation: should we test for it, and does it matter? *Journal of clinical oncology : official journal of the American Society of Clinical Oncology* *31*, 1112-1121.

- Rowell, C.A., Kowalczyk, J.J., Lewis, M.D., and Garcia, A.M. (1997). Direct demonstration of geranylgeranylation and farnesylation of Ki-Ras in vivo. *The Journal of biological chemistry* 272, 14093-14097.
- Sarthy, A.V., Morgan-Lappe, S.E., Zakula, D., Verneti, L., Schurdak, M., Packer, J.C., Anderson, M.G., Shirasawa, S., Sasazuki, T., and Fesik, S.W. (2007). Survivin depletion preferentially reduces the survival of activated K-Ras-transformed cells. *Molecular cancer therapeutics* 6, 269-276.
- Scholl, C., Frohling, S., Dunn, I.F., Schinzel, A.C., Barbie, D.A., Kim, S.Y., Silver, S.J., Tamayo, P., Wadlow, R.C., Ramaswamy, S., *et al.* (2009). Synthetic lethal interaction between oncogenic KRAS dependency and STK33 suppression in human cancer cells. *Cell* 137, 821-834.
- Shannon, P., Markiel, A., Ozier, O., Baliga, N.S., Wang, J.T., Ramage, D., Amin, N., Schwikowski, B., and Ideker, T. (2003). Cytoscape: a software environment for integrated models of biomolecular interaction networks. *Genome research* 13, 2498-2504.
- Shao, D.D., Xue, W., Krall, E.B., Bhutkar, A., Piccioni, F., Wang, X., Schinzel, A.C., Sood, S., Rosenbluh, J., Kim, J.W., *et al.* (2014a). KRAS and YAP1 converge to regulate EMT and tumor survival. *Cell* 158, 171-184.
- Shao, D.D., Xue, W., Krall, E.B., Bhutkar, A., Piccioni, F., Wang, X., Schinzel, A.C., Sood, S., Rosenbluh, J., Kim, J.W., *et al.* (2014b). KRAS and YAP1 converge to regulate EMT and tumor survival. In *Cell* (Elsevier), pp. 171-184.
- Shigematsu, H., Lin, L., Takahashi, T., Nomura, M., Suzuki, M., Wistuba, II, Fong, K.M., Lee, H., Toyooka, S., Shimizu, N., *et al.* (2005a). Clinical and biological features associated with epidermal growth factor receptor gene mutations in lung cancers. *Journal of the National Cancer Institute* 97, 339-346.
- Shigematsu, H., Takahashi, T., Nomura, M., Majmudar, K., Suzuki, M., Lee, H., Wistuba, II, Fong, K.M., Toyooka, S., Shimizu, N., *et al.* (2005b). Somatic mutations of the HER2 kinase domain in lung adenocarcinomas. *Cancer research* 65, 1642-1646.
- Singh, H., Longo, D.L., and Chabner, B.A. (2015). Improving Prospects for Targeting RAS. *Journal of clinical oncology : official journal of the American Society of Clinical Oncology* 33, 3650-3659.
- Singh, N.K., Seo, B.Y., Vidyasagar, M., White, M.A., and Kim, H.S. (2013). siMacro: A Fast and Easy Data Processing Tool for Cell-Based Genomewide siRNA Screens. *Genomics & informatics* 11, 55-57.
- Staudt, L.M. (2010). Oncogenic activation of NF-kappaB. *Cold Spring Harbor perspectives in biology* 2, a000109.

- Stein, C., Bardet, A.F., Roma, G., Bergling, S., Clay, I., Ruchti, A., Agarinis, C., Schmelzle, T., Bouwmeester, T., Schubeler, D., *et al.* (2015). YAP1 Exerts Its Transcriptional Control via TEAD-Mediated Activation of Enhancers. *PLoS genetics* *11*, e1005465.
- Stephen, A.G., Esposito, D., Bagni, R.K., and McCormick, F. (2014). Dragging ras back in the ring. In *Cancer cell*, pp. 272-281.
- Sun, M., Behrens, C., Feng, L., Ozburn, N., Tang, X., Yin, G., Komaki, R., Varella-Garcia, M., Hong, W.K., Aldape, K.D., *et al.* (2009). HER family receptor abnormalities in lung cancer brain metastases and corresponding primary tumors. *Clinical cancer research : an official journal of the American Association for Cancer Research* *15*, 4829-4837.
- Taniguchi, K., Wu, L.W., Grivennikov, S.I., de Jong, P.R., Lian, I., Yu, F.X., Wang, K., Ho, S.B., Boland, B.S., Chang, J.T., *et al.* (2015). A gp130-Src-YAP module links inflammation to epithelial regeneration. *Nature* *519*, 57-62.
- Tsai, F.D., Lopes, M.S., Zhou, M., Court, H., Ponce, O., Fiordalisi, J.J., Gierut, J.J., Cox, A.D., Haigis, K.M., and Philips, M.R. (2015). K-Ras4A splice variant is widely expressed in cancer and uses a hybrid membrane-targeting motif. In *Proc. Natl. Acad. Sci. U.S.A.*, pp. 779-784.
- Vanhaesebroeck, B., Stephens, L., and Hawkins, P. (2012). PI3K signalling: the path to discovery and understanding. In *Nat. Rev. Mol. Cell Biol.*, pp. 195-203.
- Varelas, X. (2014). The Hippo pathway effectors TAZ and YAP in development, homeostasis and disease. In *Development* (Oxford University Press for The Company of Biologists Limited), pp. 1614-1626.
- Wang, Z., Ye, J., Deng, Y., Yan, Z., Denduluri, S., and He, T.C. (2014). Wnt Hippo: A balanced act or dynamic duo? *Genes & Diseases* *1*, 127-128.
- Whitehurst, A.W., Bodemann, B.O., Cardenas, J., Ferguson, D., Girard, L., Peyton, M., Minna, J.D., Michnoff, C., Hao, W., Roth, M.G., *et al.* (2007). Synthetic lethal screen identification of chemosensitizer loci in cancer cells. *Nature* *446*, 815-819.
- Witkiewicz, A.K., McMillan, E.A., Balaji, U., Baek, G., Lin, W.C., Mansour, J., Mollaei, M., Wagner, K.U., Koduru, P., Yopp, A., *et al.* (2015). Whole-exome sequencing of pancreatic cancer defines genetic diversity and therapeutic targets. *Nature communications* *6*, 6744.
- Wuerzberger-Davis, S.M., Chen, Y., Yang, D.T., Kearns, J.D., Bates, P.W., Lynch, C., Ladell, N.C., Yu, M., Podd, A., Zeng, H., *et al.* (2011). Nuclear export of the NF-kappaB inhibitor IkappaBalpha is required for proper B cell and secondary lymphoid tissue formation. *Immunity* *34*, 188-200.

- Yamamoto, H., Shigematsu, H., Nomura, M., Lockwood, W.W., Sato, M., Okumura, N., Soh, J., Suzuki, M., Wistuba, II, Fong, K.M., *et al.* (2008). PIK3CA mutations and copy number gains in human lung cancers. *Cancer research* 68, 6913-6921.
- Yu, F.-X., Zhao, B., and Guan, K.-L. (2015a). Hippo Pathway in Organ Size Control, Tissue Homeostasis, and Cancer. In *Cell*, pp. 811-828.
- Yu, F.X., Zhao, B., and Guan, K.L. (2015b). Hippo Pathway in Organ Size Control, Tissue Homeostasis, and Cancer. *Cell* 163, 811-828.
- Yu, F.X., Zhao, B., Panupinthu, N., Jewell, J.L., Lian, I., Wang, L.H., Zhao, J., Yuan, H., Tumaneng, K., Li, H., *et al.* (2012). Regulation of the Hippo-YAP pathway by G-protein-coupled receptor signaling. *Cell* 150, 780-791.
- Zender, L., Xue, W., Zuber, J., Semighini, C.P., Krasnitz, A., Ma, B., Zender, P., Kubicka, S., Luk, J.M., Schirmacher, P., *et al.* (2008). An oncogenomics-based in vivo RNAi screen identifies tumor suppressors in liver cancer. *Cell* 135, 852-864.
- Zhang, D., Ma, X., Sun, W., Cui, P., and Lu, Z. (2015). Down-regulated FSTL5 promotes cell proliferation and survival by affecting Wnt/beta-catenin signaling in hepatocellular carcinoma. *International journal of clinical and experimental pathology* 8, 3386-3394.
- Zhao, B., Kim, J., Ye, X., Lai, Z.C., and Guan, K.L. (2009). Both TEAD-binding and WW domains are required for the growth stimulation and oncogenic transformation activity of yes-associated protein. *Cancer research* 69, 1089-1098.
- Zhao, B., Li, L., Lei, Q., and Guan, K.L. (2010a). The Hippo-YAP pathway in organ size control and tumorigenesis: an updated version. *Genes & development* 24, 862-874.
- Zhao, B., Li, L., Tumaneng, K., Wang, C.Y., and Guan, K.L. (2010b). A coordinated phosphorylation by Lats and CK1 regulates YAP stability through SCF(beta-TRCP). *Genes & development* 24, 72-85.
- Zhao, B., Ye, X., Yu, J., Li, L., Li, W., Li, S., Yu, J., Lin, J.D., Wang, C.Y., Chinnaiyan, A.M., *et al.* (2008). TEAD mediates YAP-dependent gene induction and growth control. *Genes & development* 22, 1962-1971.
- Zhong, R., Kim, J., Kim, H.S., Kim, M., Lum, L., Levine, B., Xiao, G., White, M.A., and Xie, Y. (2014). Computational detection and suppression of sequence-specific off-target phenotypes from whole genome RNAi screens. *Nucleic acids research* 42, 8214-8222.
- Zimmermann, G., Papke, B., Ismail, S., Vartak, N., Chandra, A., Hoffmann, M., Hahn, S.A., Triola, G., Wittinghofer, A., Bastiaens, P.I., *et al.* (2013). Small molecule inhibition of the KRAS-PDEdelta interaction impairs oncogenic KRAS signalling. *Nature* 497, 638-642.